1
2
3

4 **Computational pipeline provides mechanistic understanding of Omicron variant**
5 **of concern neutralizing engineered ACE2 receptor traps**
6
7
8
9

5 Soumya G. Remesh[1,2], Gregory E. Merz[2], Axel F. Brilot[2], Un Seng Chio[2], Alexandrea N. Rizo[2],
6 Thomas H. Pospiech Jr.[2], Irene Lui[1], Mathew T. Laurie[3], Jeff Glasgow[1], Chau Q. Le [1], Yun
7 Zhang[1], Devan Diwanji[2], Evelyn Hernandez[2], Jocelyne Lopez[2], Komal Ishwar Pawar[2], Sergei
8 Pourmal[2], Amber M. Smith[2], Fengbo Zhou[2], QCRG Structural Biology Consortium[#], Joseph
9 DeRisi[3,4], Tanja Kortemme[2,5,6,7], Oren S. Rosenberg[2], Anum Glasgow[8,*], Kevin K. Leung[1,*], James
10 A. Wells[1,4,9,*] & Kliment A. Verba[1,2,5,10,*]
11

12 [1] Department of Pharmaceutical Chemistry, University of California, San Francisco, San
13 Francisco, CA - 94158, USA
14 [2] QBI Coronavirus Research Group Structural Biology Consortium, University of California, San
15 Francisco, CA - 94158,
16 USA
17 [3] Department of Biochemistry and Biophysics, University of California San Francisco, San
18 Francisco, CA - 94158, USA
19 [4] Chan Zuckerberg Biohub, San Francisco, CA - 94158,
20 USA
21 [5] QBI, University of California, San Francisco, CA 94158, USA
22 [6] Department of Bioengineering and Therapeutic Sciences, University of California, San
23 Francisco, CA - 94158, USA
24 [7] The University of California, Berkeley–University of California, San Francisco Graduate
25 Program in Bioengineering, University of California, San Francisco, CA - 94158, USA
26 [8] Department of Biochemistry and Molecular Biophysics, Columbia University, New York, NY
27 10032, USA
28 [9] Department of Cellular & Molecular Pharmacology, University of California San Francisco, San
29 Francisco, CA - 94158, USA

30 [10] Lead contact

31 * Correspondence: kliment.verba@ucsf.edu, jim.wells@ucsf.edu, kevin.leung@ucsf.edu,
32 ag4522@cumc.columbia.edu

33

34

35

36

37

Summary

39 The SARS-CoV-2 Omicron variant, with 15 mutations in Spike receptor binding domain (Spike-

40 RBD), renders virtually all clinical monoclonal antibodies against WT SARS-CoV-2 ineffective.

41 We recently engineered the SARS-CoV-2 host entry receptor, ACE2, to tightly bind WT-Spike-

42 RBD and prevent viral entry into host cells ("receptor traps"). Here we determine cryo-EM

43 structures of our receptor traps in complex with full length Spike. We develop a multi-model

44 pipeline combining Rosetta protein modeling software and cryo-EM to allow interface energy

45 calculations even at limited resolution and identify interface side chains that allow for high affinity

46 interactions between our ACE2 receptor traps and Spike-RBD. Our structural analysis provides a

47 mechanistic rationale for the high affinity (0.53 - 4.2nM) binding of our ACE2 receptor traps to

48 Omicron-RBD confirmed with biolayer interferometry measurements. Finally, we show that ACE2

49 receptor traps potently neutralize Omicron- and Delta- pseudotyped viruses, providing alternative

50 therapeutic routes to combat this evolving virus.

51 **Keywords**

52 SARS-CoV-2 Omicron variant, Spike, ACE2 receptor traps, protein therapeutics, pseudovirus

53 neutralization, cryo-EM, Rosetta

54 **Introduction**

55 The rapidly evolving SARS-CoV-2 virus has accumulated several mutations throughout the

56 pandemic. The Omicron (B.1.1.529) variant was first reported in November 2021 in South Africa

57 to have 37 mutations in its Spike glycoprotein and was quickly designated as a variant of concern

58 (VOC) by the World Health Organization (Viana et al., 2022; Walls et al., 2020). The Omicron

59   Spike (S) glycoprotein receptor-binding domain (RBD) and N-terminal domain (NTD) harbor 15

60   and 11 mutations, respectively, leading to lower plasma neutralization in patients previously

61   infected with other SARS-CoV-2 variants or in fully vaccinated individuals (Cameroni et al., 2022;

62   Cao et al., 2022; Cele et al., 2021; Liu et al., 2022; Mannar et al., 2022; Planas et al., 2022;

63   VanBlargan et al., 2021; Wilhelm et al., 2021). Due to the antigenic shift in the Omicron variant,

64   currently only two out of eight clinical monoclonal antibody treatments, S309 (sotrovimab parent)

65   and the COV2-2196/COV2-2130 cocktail (cilgavimab/tixagevimab parents), retain appreciable

66   neutralizing capacity albeit reduced by 2-3 and 12-200 fold, respectively compared to

67   neutralization of Wuhan-hu-1 strain (Cameroni et al., 2022; Cao et al., 2022; Liu et al., 2022;

68   Mannar et al., 2022; Planas et al., 2022; VanBlargan et al., 2021). An earlier VOC, the B.1.617.2

69   Delta variant, also acquired 10 mutations in the Spike S glycoprotein, outcompeted other

70   circulating virus isolates, and enhanced transmission and pathogenicity while diminishing

71   antibody-based neutralization activity (McCallum et al., 2021; Mlcochova et al., 2021).

72   Interestingly, both the Delta- and Omicron RBD continue to bind the SARS-CoV-2 entry receptor,

73   human angiotensin converting enzyme 2 (ACE2), with almost 2-fold higher affinity than the wild-

74   type Spike-RBD (Cameroni et al., 2022; Mannar et al., 2022). Previously, we developed

75   engineered ACE2 "receptor traps" as viable candidates for SARS-CoV-2 virus neutralization

76   (Glasgow et al., 2020). The receptor traps were computationally designed and further affinity-

77   optimized by yeast display. The optimized ACE2 extracellular domains were fused to a human

78   IgG1 Fc domain to afford additional binding avidity and neonatal Fc receptor (FcRN) binding for

79   long circulating half-life. One advantage of using an ACE2 receptor trap as a therapeutic to treat

80   SARS-CoV-2 infections is that resistance evolved to ACE2 traps would also likely render the virus

81   unable to infect host cells via the ACE2 entry receptors. Thus, ACE2 traps could provide

82   alternative therapeutic strategies for the rapidly evolving SARS-CoV-2 virus.

83   Our computationally designed (CVD293) and affinity matured (CVD313) ACE2 Fc-fusions have

84 ~20-25-fold improved virus neutralization ability against WT-SARS-CoV-2 pseudotyped lentivirus

85 (Wuhan-hu-1 strain) compared to the WT-ACE2 Fc-fusion (Glasgow et al., 2020). However, the

86 structures of neither CVD293 nor CVD313 bound to WT-Spike-RBD have been captured, leaving

87 it an open question as to why the affinity matured ACE2 receptor traps bind WT-Spike-RBD

88 tighter. Here, we shortened the length of the linker between the ACE2 extracellular domain

89 (residues 18-740) of CVD313 and the Fc domain to ~13 amino acids to generate the construct

90 CVD432, which has an improved mammalian expression profile (total yield post purification of

91 CVD432 is ~2.5 times more than CVD313). We determined the cryo-EM structures of wild-type

92 full-length Spike protein (WT-fl-Spike) with either CVD293 or CVD432, which revealed molecular

93 details of the interactions between the ACE2 receptor traps and fl-Spike. Building on previous

94 approaches to provide ensemble models from cryo-EM maps (Herzik et al., 2019), we developed

95 a multi-model workflow to improve our confidence in the molecular interactions and the interaction

96 energies of the ACE2/RBD. This analysis allowed us to detect subtle interface differences

97 between the two receptor traps that were critical for the improved ACE2/RBD interface.

98 Furthermore, we used the cryo-EM structures together with Rosetta interface energy calculations

99 to model the interactions between our ACE2 receptor traps and Spike-RBD of Omicron VOC of

100 SARS-CoV-2, rapidly identifying the direct contact residues and predicting an even tighter

101 interaction than to the Spike-RBD of Wuhan-hu-1 strain. We validated these structural modeling

102 results by performing biolayer interferometry measurements. Finally, we showed that our ACE2

103 receptor traps potently neutralize Delta- and Omicron-SARS-CoV-2 pseudotyped viruses and

104 thus can serve as alternate therapeutic candidates against SARS-CoV-2 infections.

105

106 **Results**

107

108 **Cryo-EM reconstructions of WT-fl-Spike trimer in complex with engineered ACE2 receptor**

109 **traps**

110

111 To understand the molecular details of the interactions between the WT-fl-Spike and the

112 engineered ACE2 receptor traps CVD293 and CVD432, we determined the cryo-EM structures

113 of these complexes (Figure 1). We confirmed that both CVD293 and CVD432 potently neutralize

114 WT-SARS-CoV-2 (Wuhan-hu-1 B.1 strain with D614G mutation only) pseudotyped virus (Figure

115 S1d). As noted previously for the WT-fl-Spike/WT-ACE2 complex (Yan et al., 2021; Zhou et al.,

116 2020a), we observed conformational heterogeneity for the complexes between WT-fl-Spike and

117 the engineered ACE2 receptor traps, with the number of RBDs in the "up" or "down" conformation

118 per spike protein varying in the ACE2-bound state. The complex between WT-fl-Spike and

119 CVD293 showed a 1-RBD-up WT-fl-Spike with full ACE2 occupancy (~20%), an appreciable

120 percentage of 1-RBD-up WT-fl-Spike with partial ACE2 occupancy (~54%), a 2-RBD-up state with

121 1-ACE2 occupancy (~15%) and a 1-RBD-up state with no ACE2 occupancy (Figure 1a) per trimer.

122 On the other hand, WT-fl-Spike and CVD432 showed a 1-RBD-up WT-fl-Spike with full ACE2

123 occupancy (~12%), a 2-RBD-up state with 2-ACE2 occupancy (~9%), all-RBD-down state, and

124 other partial- to no-ACE2 occupancy 1-RBD- and 2-RBD-up states (Figure 1b). While ACE2

125 residues 18-614 were well resolved and could be fit into our cryo-EM maps of the complexes

126 between WT-fl-Spike/ACE2 receptor traps, we could not model the highly flexible collectrin

127 domain of the ACE2 traps (residues 615-740) as well as the Fc-domains. Nevertheless, the WT-

128 Spike-RBD/ACE2 receptor trap sub-region could be resolved at low to medium resolution.

129

130 Local refinement of CVD293 or CVD432 (residues 18-614) with WT-Spike-RBD (residues 330-

131 541, Wuhan-hu-1 strain) generated maps of resolution ~3.8-4.8 Å and 3.4-3.8 Å, respectively, for

132 the interface residues (Figure 2a, S2, S3, S4 and S5). As described above, the high level of

133 heterogeneity between the 1-RBD-up and 2-RBD-up states for WT-fl-Spike with either CVD293

134 or CVD432 made obtaining high resolution maps of the interface residues challenging. To better

135 understand the modalities of continuous protein motions within the 1-RBD-up or 2-RBD-up states,

136   we utilized 3D variability analyses (3DVA) (Punjani and Fleet, 2021) (Figure S1a-c). Both WT-fl-

137   Spike/CVD293 and WT-fl-Spike/CVD432 complexes showed considerable rotation relative to the

138   vertical axis (~5-7°) in the 1-RBD-up/ACE2 bound sub-region of the cryo-EM map (Figure S1a,

139   b). In contrast, the 2-RBD-up state of WT-fl-Spike/CVD432 showed lateral shift of the ACE2 bound

140   RBD sub-region of the cryo-EM map relative to the vertical axis of rotation (Figure S1c). This high

141   degree of variability in the ACE2 bound/RBD sub-region of the cryo-EM map further impeded high

142   resolution structure determination of the interface residues. Consequently, the precise rotamer

143   positions, especially of key interface residues for CVD293 (engineered mutations - K31F, H34I,

144   E35Q) or CVD432 (engineered mutations - K31F, N33D, H34S, E35Q) could not be obtained with

145   high confidence directly from the cryo-EM maps. (Figure 2b, c; cryo-EM consensus models are

146   shown fit to the cryo-EM maps).

147

148   Improving confidence of the interface interactions in limited resolution cryo-EM maps

149   through Rosetta enabled multi-model workflow

150

151   Inspired by a previous ensemble model refinement approach to improve confidence in maps with

152   resolution variation (Herzik et al., 2019), we developed a multi-model workflow which allowed for

153   calculation of an "average predicted interface energy" metric across an ensemble of models

154   consistent with the cryo-EM map in addition to the previously reported "average RMSD" metric.

155   Together, these metrics provided a statistics-based view of the ACE2/RBD interface (Figure 3a).

156   Briefly, 10-residue overlapping stretches of the ACE2 interface helix (residues 21 - 52) of each

157   cryo-EM consensus model (WT-Spike-RBD (330-541)/CVD293 (18-614) or WT-Spike-RBD (330-

158   541)/CVD432 (18-614)) were subjected to a CartesianSampler mover within Rosetta that samples

159   similar sequence and secondary structure fragments from within PDB and locally minimizes them

160   into the cryo-EM density, generating 2000 models for each 10-residue stretch. Each model was

161   then all-atom minimized within the cryo-EM map using FastRelax mover with a scoring term for

162   the model agreement with the cryo-EM map, as previously described (DiMaio et al., 2015). The

163   Rosetta parameters and scoring functions used were based on the estimated map resolution

164   (Wang et al., 2016). This refinement protocol was iteratively run to generate a total of ~8000

165   overlapping atomic models of the interface helix.

166

167   We next ranked the atomic models based on total Rosetta scores ensuring good geometries (pick

168   top 200) and fits to the cryo-EM map (pick top 20 out of the above 200) for each 10-residue stretch

169   to select a total of 80 models for the entire interface helix. The average per residue side-chain

170   RMSDs and predicted average interface energy for all the residues of the interface helix for the

171   top selected cryo-EM based models were then calculated (Figure 3b,e). We compared average

172   per-residue side-chain RMSDs as we expected very small changes in the average backbone

173   RMSDs which can cause side-chain discrepancies being down-weighted in average full-

174   residue RMSDs. We superimposed the interface helix residues (residues 21-52) of the top 80

175   selected cryo-EM based models for both CVD293 and CVD432 to analyze the convergence of

176   the side-chain conformations and the intermolecular interaction with corresponding WT-Spike-

177   RBD residues. We observed that while the interface residues of CVD293 (F31, I34) or CVD432

178   (F31) with low average side-chain RMSD make well-defined hydrophobic interactions with

179   corresponding residues in WT-Spike-RBD (L455, F456, Y489), the high average side-chain

180   RMSD residue (Q35 of both CVD293 and CVD432) makes hydrogen bond interactions with

181   neighboring WT-Spike-RBD residue (Q493) in over 90% of the atomic models (Figure 3c, d). We

182   further noted that CVD432 high average side-chain RMSD residue, S34, can make both inter-

183   (with WT-Spike-RBD residue Y453) and intra-molecular hydrogen bonds (with backbone carbonyl

184   atoms of residues D30 or F31). We infer that the low average side-chain RMSD engineered

185   hydrophobic residues of the ACE2 receptor traps likely provide the key functional interactions

186   responsible for the improved binding affinity of the engineered receptor traps for WT-Spike-RBD.

187

188

Analysis of the cryo-EM based models of CVD293 (18-614) and CVD432 (18-614) in complex with the WT-Spike-RBD (330-541)

191

The comparison between the original computationally designed model of the CVD293/WT-Spike-RBD complex and the cryo-EM based models of the complex determined with our multi-model workflow revealed high overall structural agreement (Figure 2d). The average Cα-RMSD between the computationally designed model and the experimentally solved cryo-EM consensus model of CVD293 (residues 18-614) was 0.93 Å, and the average Cα-RMSD for the interface helix (ACE2 residues 21-88, 322-329, 352-358 and Spike residues 444-446, 475-505) was 0.41 Å.

198

We next compared the calculated interface energy for the CVD293/WT-Spike-RBD interface in the design model and the cryo-EM based models. We found that the predicted interface energy is considerably lower for the CVD293 design model (-58 REU) than the average of 80 CVD293 cryo-EM based models (-45 REU) (Figure 3e). This discrepancy between the predicted interface energy for the design model and the average interface energy calculated from the 80 cryo-EM based models is likely due to several differences in side-chain-mediated interactions involving designed residues. For example, isoleucine 34, a designed residue in CVD293, is predicted to contribute less to the interface energy in the cryo-EM based models (average from 80 atomic models of CVD293: -2.5 REU) than in the design model (-3 REU), despite strong agreement in the atomic coordinates for this residue across all cryo-EM based models (Figure 2d). The predicted interaction energy of I34 is worse in the cryo-EM models than the design model because its interaction partner across the interface, residue L455 of WT-Spike-RBD, universally adopts a different rotamer than the one in the original design model (Figure S7a).

212

213 Residue Q35, another designed residue in CVD293, showed the largest observed average per-

214 residue side-chain RMSD among the designed positions on ACE2 in the cryo-EM based models

215 (Figure 3b). Although the Q35 side-chain often occupies a different rotamer in the cryo-EM based

216 models than in our original design model of CVD293, it still makes a hydrogen bond with the WT-

217 Spike-RBD residue Q493 as intended (Figure 3c). The WT-Spike-RBD residue Q493 shows

218 minimal conformational heterogeneity across the 80 cryo-EM based models of the complex

219 CVD293/WT-Spike-RBD, and it makes intramolecular hydrogen bonds with the carbonyl group of

220 the WT-Spike-RBD residue F490 to maintain the same loop conformation as seen in the complex

221 between WT-ACE2 and WT-Spike-RBD (Figure S7a). It is plausible that the minimal average

222 side-chain RMSD of residue Q493 and the overall similar loop conformation around residues

223 F490-Q493 in the complex CVD293/WT-Spike-RBD contribute to the observed conserved

224 hydrogen bond with residue Q35.

225

226 Another WT-ACE2 residue, K31, was mutated to a phenylalanine in CVD293. Consequently, the

227 hydrogen bond between the WT-ACE2 residue K31 and the WT-Spike-RBD residue Q493 was

228 lost in the complex CVD293/WT-Spike-RBD. Instead of making this hydrogen bond, the designed

229 residue F31 in CVD293, with less than 1 Å average observed average side-chain RMSD, makes

230 good packing interactions with other aromatics at the WT-Spike-RBD/engineered ACE2 trap

231 interface as expected (Figure 3c). Overall, the average Cα-RMSD between the computationally

232 designed model and the experimentally solved cryo-EM consensus model of CVD293 (residues

233 18-614) is close to 1 Å. However, using the cryo-EM based models of complex CVD293/WT-

234 Spike-RBD determined with our multi-model workflow, specific residue-pair interactions that were

235 critical to improving the WT-ACE2/WT-Spike-RBD interface with our computational design

236 strategy are revealed.

237

238 We next wanted to understand why the affinity maturation of CVD293 in our yeast surface display

239 campaign resulted in the I34S interface mutation in the construct CVD432, which has improved

240 binding affinity for WT-Spike-RBD. We first generated a CVD432 "design" model by mutating the

241 residue I34 in the CVD293 cryo-EM consensus model to a serine *in silico*. We also made an N33D

242 mutation to CVD293 *in silico* even though this position is outside the RBD binding interface,

243 because this mutation was also identified by yeast surface display in CVD432. The calculated

244 interface energy for the CVD432 design model/WT-Spike-RBD interface is higher (-47 REU) than

245 the average interface energy from 80 cryo-EM based models of the complex CVD432/WT-Spike-

246 RBD (-53 REU) (Figure 3e). It can be inferred that simple *in silico* mutations do not provide a full

247 explanation for the improved binding affinity between the engineered ACE2 trap and the WT-

248 Spike-RBD, highlighting the value of the cryo-EM structure solution.

249 Comparing the cryo-EM based models of the complexes CVD293/WT-Spike-RBD and

250 CVD432/WT-Spike-RBD, we find that the calculated interface energy from the average of 80 cryo-

251 EM based models of the complex CVD432/WT-Spike-RBD is lower (-53 REU) than the average

252 of 80 cryo-EM based models of the complex CVD293/WT-Spike-RBD (-45 REU) (Figure 3e). The

253 decrease in calculated interface energy for the cryo-EM based models of the complex

254 CVD432/WT-Spike-RBD as compared to that of the complex CVD293/WT-Spike-RBD is

255 surprising for three reasons. First, S34 can adopt several different conformations (Figure 3d).

256 Secondly, S34 makes weaker energetic contributions to the interface energy in all of the cryo-EM

257 based models of the complex CVD432/WT-Spike-RBD than I34 in the complex CVD293/WT-

258 Spike-RBD, regardless of the serine rotamer (Figure S6a). Third, S34 in CVD432 also has a

259 higher average per-residue energy than I34 in CVD293 (Figure S6b). It is possible that a serine

260 was enriched at position 34 in our directed evolution campaign using error-prone PCR because

261 of the isoleucine parental codon, from which single base mutations could only lead to large

262 hydrophobic amino acids, serine, threonine, or asparagine. Of these possibilities, serine is the

263 smallest amino acid, and might have been favored simply to allow the other ACE2 residues to

264 maintain favorable interactions with the RBD.

It appears that no individual residue at the interface is fully responsible for the improved interface energy in CVD432 cryo-EM based models over the CV293 design; rather, this improvement is the sum of several small improvements among many residues at the interface (Figure S6a). Interestingly, CVD432 contains an N33D mutation away from the interface which may be responsible for such overall stabilization of the interface. In all our models, N33D mutation breaks a hydrogen bond with the Q96 side-chain within ACE2 yielding a subtle shift of the neighboring residues towards the RBD (Figure S7b). This is correlated with subtly lower interface energies for these residues and lower total energy for D33 (Figure S6b, c). The N33D mutation was also observed to improve the RBD binding interaction in another ACE2 engineering study (Chan et al., 2020) and a computational analysis of ACE2 mutations (Chowdhury et al., 2020). Additionally, the interface helix may be stabilized by the main chain-side chain hydrogen bond between the S34 hydroxyl group and the F31 backbone carbonyl group in ACE2 (Figure 3d) that is not appropriately scored by Rosetta. Altogether, the improved SARS-CoV-2 neutralization by CVD432 compared to CVD293 is driven by mutations at the interface that improve binding in addition to stability-enhancing mutations outside the interface. As such, both protein stability and interface preorganization contribute to the overall stability of the receptor trap-RBD complex.

ACE2 receptor traps bind Omicron-RBD with increased affinity and neutralize the SARS-CoV-2 VOC

Several of the 37 Omicron Spike mutations have been observed in other SARS-CoV-2 variants. For example, previous reports suggest that the N501Y mutation increases WT-ACE2 binding affinity while the K417N mutation decreases the WT-ACE2 binding affinity in some SARS-CoV-2 variants (Barton et al., 2021; Laffeber et al., 2021; Liu et al., 2021; Mannar et al., 2021; Tian et al., 2021; Zhu et al., 2021). Fourteen of the 37 mutations have not been reported previously in

291 other variants but together were reported to improve the binding affinity ~2-3 fold between

292 Omicron-RBD and WT-ACE2 (Cameroni et al., 2022; Mannar et al., 2022; McCallum et al., 2022).

293 For example, while the Y505H mutation leads to loss in hydrogen bond interactions with WT-

294 ACE2 residue E37, there are several compensatory mutations in the Omicron-RBD. These

295 include Q493R and G496S, which result in new hydrogen bonds with WT-ACE2 residues E35

296 and K353, respectively and several others (Table S1, residue pairs colored green).

297

298 Our ACE2 receptor traps have >170-fold improved binding affinity for monomeric WT-Spike-RBD

299 compared to the binding affinity of WT-ACE2 for WT-Spike-RBD (Glasgow et al., 2020). To

300 evaluate if our ACE2 receptor traps would bind Omicron-RBD, we first generated models of

301 Omicron-RBD (330-530)/CVD293 (18-614) and Omicron-RBD (330-530)/CVD432 (18-614) by

302 superimposing and replacing WT-Spike-RBD in our respective cryo-EM local refinement of the

303 complexes with Omicron-RBD from the recently determined cryo-EM structure of Omicron-Spike

304 (330-530)/WT-ACE2 (19-613) (PDB ID: 7T9L, EMD-25761) (Figure 4a,b, panels on the right);

305 figure S8) and minimizing the complexes. Next, we calculated the Rosetta interface energies of

306 these models (Figure 4a,b; panels on the left). Although we predict an energy penalty for

307 engineered interface interaction residue pairs going from R493/E35 in Omicron-RBD/WT-ACE2

308 to R493/Q35 in Omicron-RBD/CVD293 or Omicron-RBD/CVD432 (in red in Figure 4a-b; panels

309 on the left), overall, we also predict improved binding affinities between the Omicron-RBD and

310 the engineered ACE2 receptor traps. Total interface energy for the interface residue pairs

311 contributing to the affinity between CVD293 or CVD432 to Omicron-RBD was calculated to be -

312 10.77 REU and -8.5 REU, respectively. For reference, the total interface energy for the interface

313 residue pairs contributing to the affinity between WT-ACE2 and Omicron-RBD was calculated to

314 be -4.99 REU. Potential contributions from interaction residue pairs L455/F31, Y489/F31 and

315 F31/R493 (in yellow in Figure 4a-b; panels on the left) and other residue pair interactions between

316 residue I34 of CVD293 or S34 of CVD432 and L455 of Omicron-RBD may be improving the

317   interface affinity (in blue in Figure 4a-b; panels on the left).

318

319   To test whether improved predicted interface energies correspond to increased apparent binding

320   affinities, we assayed the binding affinity of CVD293 and CVD432 for Omicron-RBD by performing

321   biolayer interferometry (BLI). The BLI-determined dissociation constant (K_D) between Omicron-

322   RBD/CVD293 (K_D = 4.2 nM) or Omicron-RBD/CVD432 (K_D = 0.53 nM) were measured to be 10-

323   and 100-fold lower than that for Omicron-RBD/WT-ACE2(18-740)-Fc-fusion, respectively (Figure

324   4c, Figure S9, Table S2). The hydrophobic interactions specific to Omicron-RBD/ACE2 receptor

325   trap complexes, along with the several compensatory mutations in Omicron-RBD/ACE2 interface

326   that are also maintained with the ACE2 receptor traps, likely result in the BLI-measured improved

327   affinity. Interestingly, CVD293 and CVD432 showed similar (K_D = 1.9 nM) or about 100-fold (K_D =

328   0.071 nM) lower K_D for Delta-RBD, respectively.

329

330   Finally, to determine whether the improved in vitro binding affinity also leads to higher potency in

331   viral neutralization, we tested the neutralization of Omicron (B.1.1.529) and Delta (B.1.617.2)

332   SARS-CoV-2 variants by our ACE2 receptor traps in pseudoviruses bearing these variants of

333   interest generated using recombinant vesicular stomatitis virus (VSV) expressing green

334   fluorescent protein (GFP) in place of the VSV glycoprotein (rVSV ΔG-GFP). We compared the

335   neutralization of Delta and Omicron pseudoviruses to a control Spike-WT pseudovirus with a

336   D614G mutation. The pseudovirus neutralization assays demonstrated that both CVD293 and

337   CVD432 neutralize Delta (IC50 = 1.4 nM, 1.6 nM, respectively) and Omicron (IC50 = ND, 0.15nM,

338   respectively) pseudoviruses, with IC50 values improved between 2-20-fold over Spike-WT (IC50

339   = 2.6 nM, 3.7 nM, respectively) pseudovirus (Figure 4d). Taken together, the results from the BLI

340   and pseudovirus neutralization assays suggest that our engineered ACE2 traps, although

341   computationally designed and affinity improved against WT-Spike-RBD, can still bind the rapidly

342   evolving SARS-CoV-2 variants with high affinity and potently block virus entry into cells.

Discussion

Over the course of the current pandemic, several neutralizing monoclonal antibodies (mAbs) have been identified and some have been evaluated clinically as therapeutic candidates against SARS-CoV-2 infection (Barnes et al., 2020a; Baum et al., 2020; Cohen et al., 2021; Dong et al., 2021; Gottlieb et al., 2021; Hansen et al., 2020; Jones et al., 2021; Shi et al., 2020; Zost et al., 2020). These mAbs are broadly categorized based on their ability to bind RBD in the "up" or "down" conformations on fl-Spike, engaging epitopes that can or cannot block ACE2 receptor binding to the RBD (Barnes et al., 2020b, 2020a; Liu et al., 2020; Shi et al., 2020; Tortorici et al., 2020). Several of the mAbs that bind the ACE2 recognition site (also called the receptor binding motif, RBM) within the RBD lost in-vitro neutralization activity against the Omicron-VOC (Cameroni et al., 2022; Mannar et al., 2022; Park et al., 2022). Interestingly, only the S2K146 mAb that binds SARS-CoV-2, SARS-CoV and other sarbecoviruses through ACE2 molecular mimicry retained neutralization activity against the Omicron-VOC (Cameroni et al., 2022; Park et al., 2022). This suggests that ACE2 specific binding epitope residues have a higher barrier for emergence of escape mutants.

We (Glasgow et al., 2020) and others (Chan et al., 2020; Higuchi et al., 2021; Lei et al., 2020) have explored "ACE2 decoy receptors" or "ACE2 receptor traps" that bind and block the RBD as an alternative approach for SARS-CoV-2 virus neutralization. Our ACE2 receptor traps were computationally designed, and affinity matured against the WT-Spike-RBD. In this study, we first determined the cryo-EM structures of the ACE2 receptor traps with the WT-fl-Spike to validate the mechanism of action for our computationally designed trap and to determine the molecular basis for the additional binding affinity improvement by the affinity-matured trap. Although the cryo-EM structures were informative, the limited resolution of ACE2/Spike-RBD interface residues prompted us to explore a multi-model cryo-EM structural workflow to circumvent the limited

369 resolution and leverage model ensembles for interface energy calculations.

370

371 From the cryo-EM structures and the derived multi-model workflow, we learned key lessons for

372 designing strong binders: that distributed binding interactions across a protein-protein interface

373 are more effective as compared to reliance on one or two important cross-interface interactions;

374 and that it is important to prioritize the stability of all proteins individually in addition to the protein

375 complex. Importantly, such stability may come from substitutions away from directly interacting

376 residues, like N33D mutation in CVD432 that yields a lower energy conformation for that residue

377 allowing for lower interface energies of surrounding residues. The data suggest that the stability

378 and pre-organization of each protein at the interface is as important as the cross-interface

379 interactions in the overall stability of the complex.

380

381 Recently, two engineered ACE2 decoy receptors have been reported to broadly neutralize SARS-

382 CoV-2 variants including the Omicron-VOC (Ikemura et al., 2021; Zhang et al., 2022). These

383 engineered decoy receptors neutralized the Omicron-VOC with IC50s comparable or even better

384 than Omicron-VOC neutralizing mAbs such as VIR-7831. Apeiron's APN01, a wild-type ACE2

385 soluble extracellular domain, has also shown promising results in early-phase clinical trials and

386 retains the ability to neutralize multiple variants of concern (Wirnsberger et al., 2021).

387 Furthermore, in a laboratory simulation of viral mutation under neutralizing selective pressure,

388 another engineered ACE2 decoy receptor, 3n39v2 retained its neutralizing capacity over several

389 passage cycles (Higuchi et al., 2021). Thus, soluble engineered ACE2 receptors have therapeutic

390 value against SARS-CoV-2 variants and may continue to be relevant as this virus evolves further.

391

392 Application of the multi-model workflow increased our confidence in the atomic positions of

393 computationally designed amino acids at the ACE2-Spike interface. This laid the groundwork for

394 further improvements in the receptor trap design and allowed us to model interactions of the

395 receptor traps with the Omicron-RBD. We experimentally verified the Omicron-RBD binding

396 interactions with the receptor traps using BLI and pseudovirus neutralization assays,

397 demonstrating that our ACE2 receptor traps designed for neutralization of WT-fl-Spike from

398 SARS-CoV-2 remain robust to dozens of mutations in the VOCs. This is both surprising and

399 exciting since our computational design and affinity maturation optimized the binding interface of

400 ACE2 to selectively bind the targeted antigen, WT-Spike-RBD. These results are also in contrast

401 to pan-specific antibodies that are affinity matured to be highly epitope- or antigen-specific binders

402 (Koerber et al., 2013; Mou et al., 2018; Zhou et al., 2020b). Perhaps, the particular hydrophobic

403 mutations at the binding interface of our ACE2 receptor traps make them more adaptable to Spike-

404 RBD mutations. Alternatively, as the virus evolves, its affinity for its entry receptor increases and

405 fortuitously also to our ACE2 receptor traps.

406

407 In addition to the RBM antigenic site, other mAbs with antigenic sites outside the RBM such as

408 Sotrovimab, S309, S2X259 and S2H97 also retained neutralization activity against Omicron-VOC

409 (Cameroni et al., 2022; Mannar et al., 2022; McCallum et al., 2022). A bifunctional antibody format

410 called ReconnAbs (receptor-blocking conserved non-neutralizing antibodies) was recently shown

411 to convert non-neutralizing antibodies to potent neutralizers of SARS-CoV-2 VOCs by linking the

412 "WT-ACE2 receptor" to a bispecific antibody targeting two non-overlapping conserved epitopes

413 (Weidenbacher et al., 2022). We envision future versions of our ACE2-receptor trap binders to be

414 knob-in-hole bispecifics and other Fc-fusion formats with one engineered ACE2 arm and other

415 arm(s) as mAbs with antigenic sites outside the RBM, other non-neutralizing mAbs or Vh domains.

416

417 Overall, this study exemplifies how technical advances in cryo-EM and computational protein

418 design methods can be combined towards improving the *design-build-test* cycle for engineering

419 potent biotherapeutics, even for difficult targets such as the ACE2 complex with the SARS-CoV-

420 2 Spike protein. Furthermore, this workflow can be generalized for solving the cryo-EM structures

421 of other protein complexes and improving computational protein design protocols.

422

Acknowledgements

424

432 The structural biology portion of this work was performed by the QCRG (Quantitative Biosciences

433 Institute Coronavirus Research Group) Structural Biology Consortium. Listed below are the

434 contributing members of the consortium listed by teams in order of team relevance to the

435 published work. Within each team the team leads are italicized (responsible for organization of

436 each team, and for the experimental design utilized within each team), then the rest of team

437 members are listed alphabetically.

438 **QCRG Structural Biology Consortium**

439 **CryoEM grid freezing/collection team**: *Axel F. Brilot, Gregory E. Merz, Alexandrea N. Rizo,*

440 Caleigh M. Azumaya, Julian R. Braxton, Meghna Gupta, Fei Li, Kyle E. Lopez, Arthur Melo, Frank

441 Moss, Joana Paulino, Thomas H. Pospiech Jr., Sergei Pourmal, Cristina Puchades, Amber M.

442 Smith, Ming Sun, Paul V. Thomas, Feng Wang & Zanlin Yu

443 **CryoEM data processing team:** *Axel F. Brilot, Gregory E. Merz, Alexandrea N. Rizo, Soumya*

444 *G. Remesh,* Daniel Asarnow, Julian R. Braxton, Melody G. Campbell, Cynthia M. Chio, Un Seng

445 Chio, Miles Sasha Dickinson, Devan Diwanji, Bryan Faust, Meghna Gupta, Nick Hoppe, Mingliang

446 Jin, Fei Li, Junrui Li, Yanxin Liu, Henry C. Nguyen, Joana Paulino, Thomas H. Pospiech Jr., Sergei

447 Pourmal, Smriti Sangwan, Raphael Trenker, Donovan Trinidad, Eric Tse, Kaihua Zhang & Fengbo

448 Zhou

449 **Mammalian cell expression team:** *Evelyn Hernandez, Devan Diwanji, Amber M. Smith,*

450 Caleigh M. Azumaya, Christian Billesboelle, Alisa Bowen, Melody G. Campbell, Nick Hoppe,

451 Yen-Li Li, Edmond Linossi, Jocelyne Lopez, Phuong Nguyen, Carlos Nowotny, Quynh Mai,

452 Hevatib Mehmood, Michael Paul, Cristina Puchades, Mali Safari, Smriti Sangwan, Kaitlin

453 Schaefer, Raphael Trenker, Tsz Kin Martin Tsui, Natalie Whitis & Jianhua Zhao

454 **Protein purification team:** *Michelle Moritz, Sergei Pourmal,* Daniel Asarnow, Caleigh M.

455 Azumaya, Cynthia M. Chio, Bryan Faust, Meghna Gupta, Raghav Kalia, Kate Kim, Tristan W.

456 Owens, Joana Paulino, Komal Pawar, Jessica K. Peters, Kaitlin Schaefer & Tsz Kin Martin Tsui

457 **Crystallography team:** *Nadia Herrera, Huong T. Kratochvil, Ursula Schulze-Gahmen, Iris D.*

458 *Young,* Justin Biel, Ishan Deshpande & Xi Liu

459 **Bacterial expression team:** *Amy Diallo, Meghna Gupta,* Jen Chen, Loan Doan, Sebastian

460 Flores, Mingliang Jin, Huong T. Kratochvil, Victor L. Lam, Yang Li, Megan Lo, Gregory E. Merz,

461 Joana Paulino, Aye C. Thwin, Erron W. Titus, Zanlin Yu, Fengbo Zhou & Yang Zhang

462 **Infrastructure team:** David Bulkley, Arceli Joves, Almarie Joves, Liam McKay, Mariano Tabios

463 & Eric Tse

464 **Leadership team:** David A. Agard, Yifan Cheng, James S. Fraser, Adam Frost, Natalia Jura,

465 Tanja Kortemme, Nevan J. Krogan, Aashish Manglik, Oren S. Rosenberg, Daniel R.

466 Southworth, Robert M. Stroud & Kliment A. Verba

467

468 **Author Contributions**

469

470 Conceptualization, K.A.V, A.G., S.G.R, T.K., K.K.L., J.A.W.; methodology (cryo-EM data

471 collection), G.E.M, A.F.B., A.N.R., T.H.P.; methodology (cryo-EM structure solution), G.E.M,

472 A.F.B., U.S.C., S.G.R.; methodology (cryo-EM based multi-model workflow), S.G.R. and K.A.V.;

473 methodology (Rosetta energy calculations), A.G.; methodology (cloning, protein expression and

474 purification), J.G., S.G.R., I.L., C.Q.L., Y.Z., E.H., D.D., S.P., A.M.S., J.L., K.I.P.; methodology

475 (Biolayer interferometry), I.L.; methodology (pseudovirus generation), M.T.L., J.D.; methodology

476 (pseudoviral assay), S.G.R.; writing—original draft, S.G.R., A.G. K.A.V., T.K., J.A.W., K.K.L.;

477 visualization, S.G.R., A.G., K.A.V.; supervision; K.A.V., A.G., K.K.L., J.A.W.; funding acquisition,

478 K.A.V., A.G., J.A.W

479

480 **Declaration of Interest**
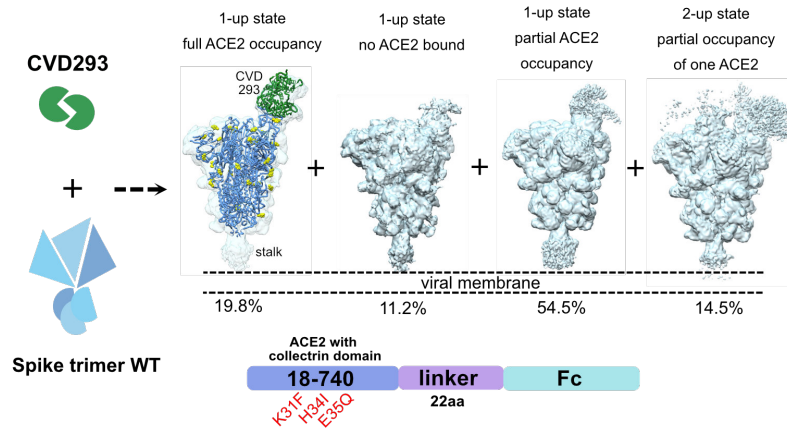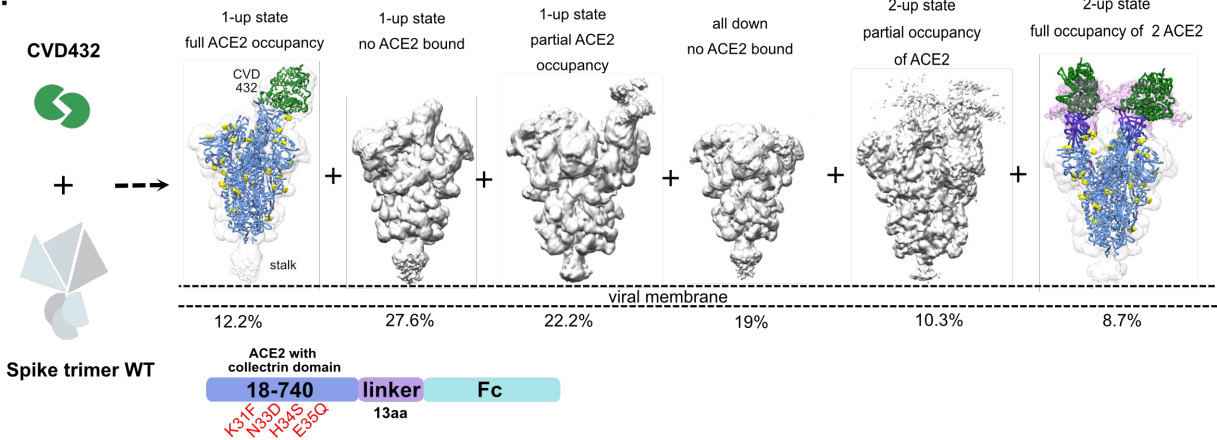
481

482 None declared

483

484

485

486

487   Figure 1.

488

Figure 1. Cryo-EM reconstruction of WT-fl-Spike with computationally designed, CVD293

or linker variant of the affinity matured variant, CVD432

a-b. Cryo-EM reconstructions of WT-fl-Spike with CVD293 or CVD432 showing the heterogeneity

in distribution of all RBD down, 1-RBD- or 2-RBD-up states and variable ACE2 occupancy. Also

shown is schematic of the primary structure of CVD293 or CVD432 and the engineered mutations,

colored by domain.

495

496

497   Figure 2.

498
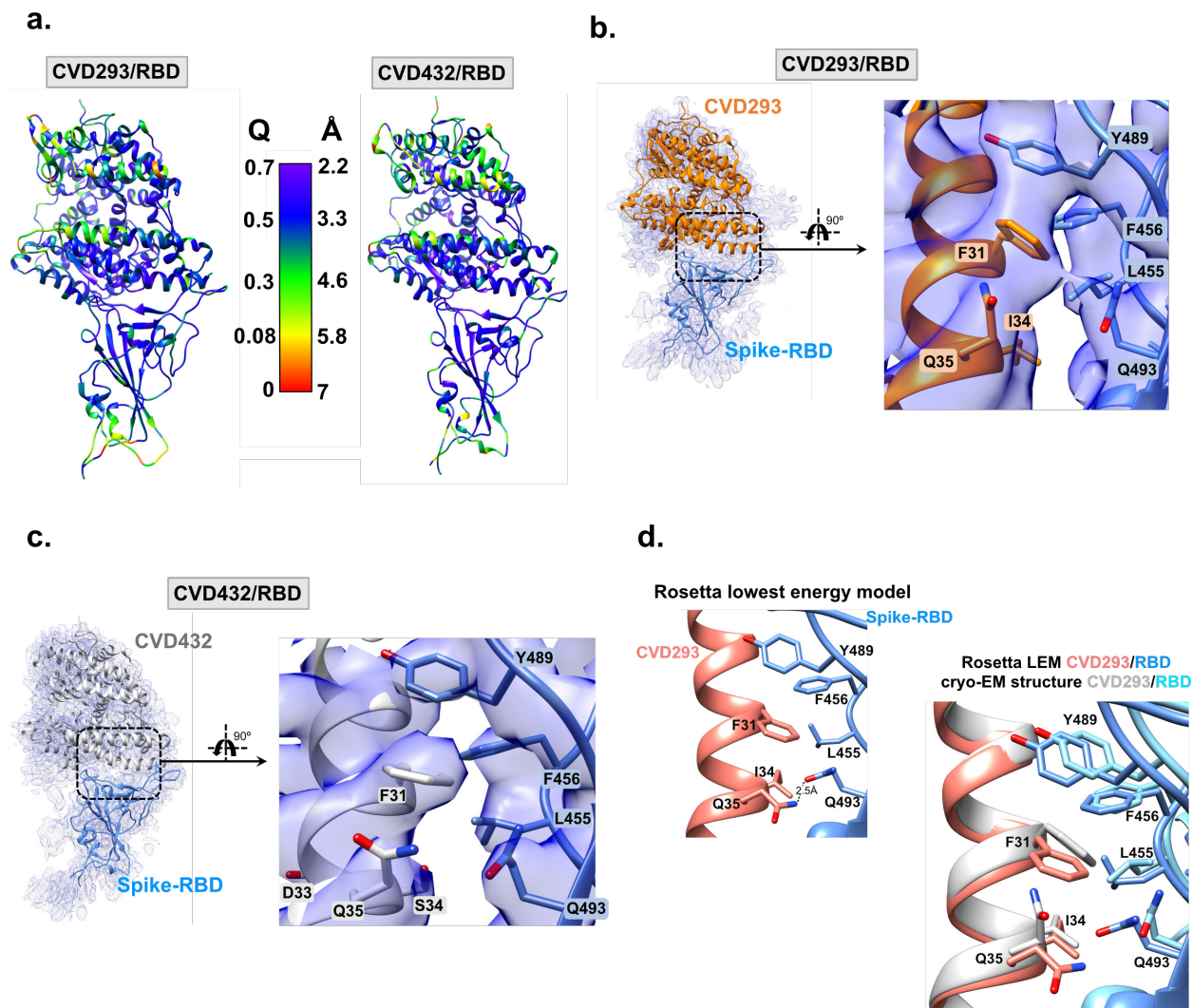
Figure 2. Cryo-EM reconstruction of WT-Spike-RBD with engineered ACE2 Fc-fusions

reveal contributions from hydrophobic interactions at RBD-ACE2 interface

a. WT-Spike-RBD/CVD293 and WT-Spike-RBD/CVD432 models colored by estimated per residue Q-score ranging from 0 (red) to 0.7 (purple). The color bar shows corresponding estimated resolution in Å for each Q-score. Expected Q-score for 3.5 Å map is 0.49 and expected Q-score for 3.36 Å map is 0.52. **b-c**. Cryo-EM reconstructions of WT-Spike-RBD with either CVD293 or CVD432 show favorable π–π stacking interactions between WT-Spike-RBD residue Y489 and engineered ACE2 residue F31. Additionally, there are also hydrophobic interactions

507   between WT-Spike-RBD residue L455 and CVD293 residue I34 are also seen. Hydrogen bond

508   interactions between WT-Spike-RBD residue Q493 and CVD293 or CVD432 residue Q35 are not

509   apparent in the cryo-EM consensus model. **d**. The Rosetta lowest energy model for CVD293 is

510   overlaid with the cryo-EM model. Both models show hydrophobic and hydrogen bond interactions

511   between CVD293 and WT-Spike-RBD residues that contribute to improved interface energy

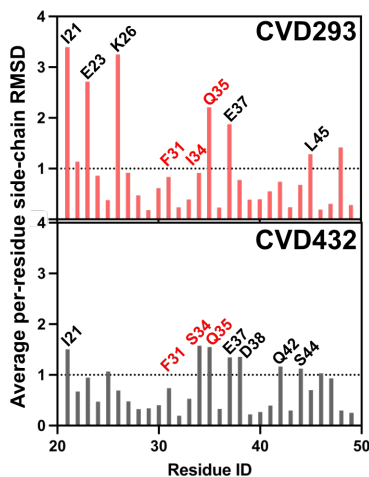512   (REU) compared to the ACE2-WT Spike RBD interaction.
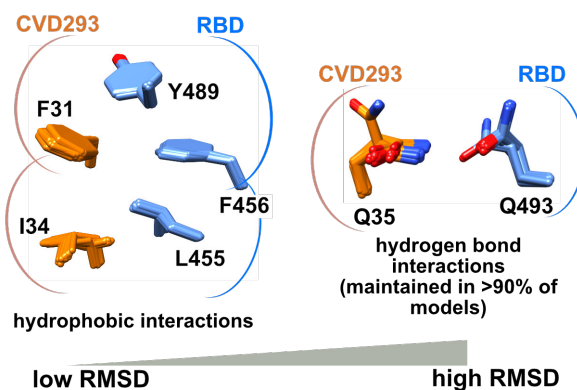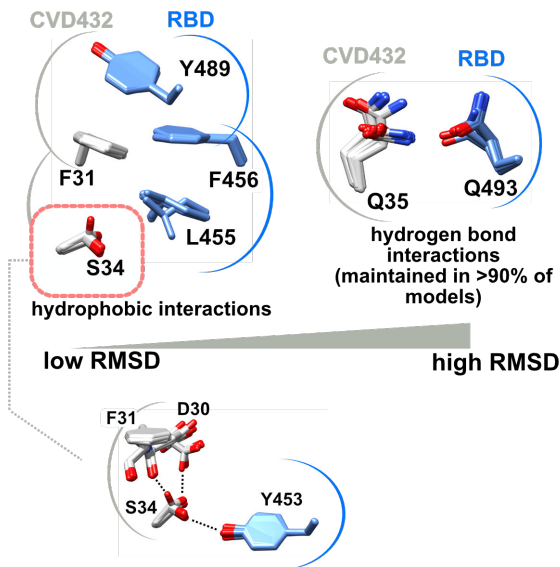
513

514

515   Figure 3.

a.
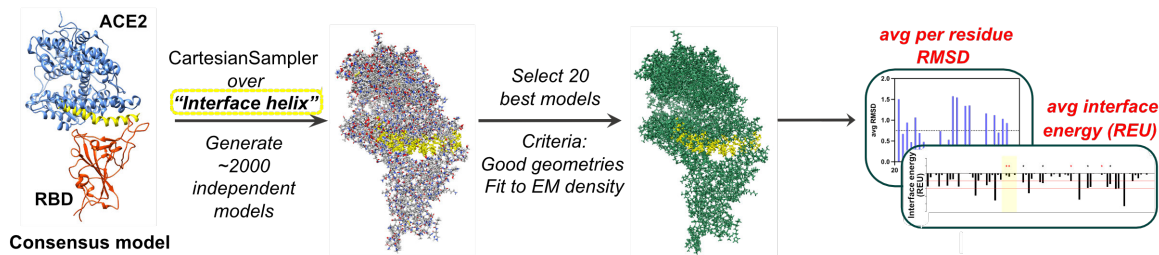
b. **Average per-residue side-chain RMSD for Interface helix**

c.

d.

e. **Interface energy**
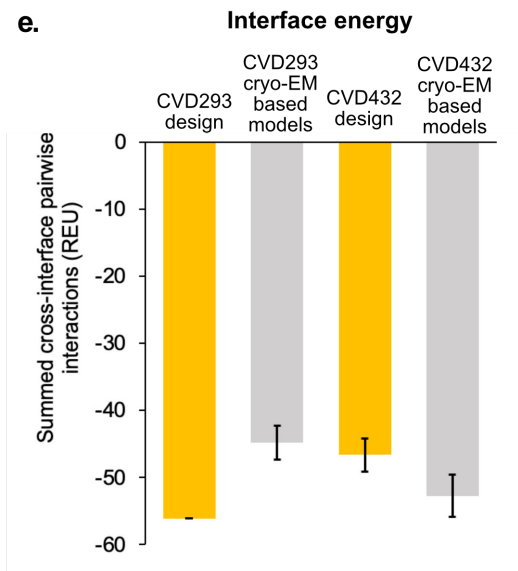
516

517 **Figure 3. Multi-model pipeline improves confidence of molecular interactions at the**

518 **interface residues in cryo-EM derived models of WT-Spike-RBD with engineered ACE2 Fc-**

519 **fusions**

520 **a.** Multi-model pipeline with average Rosetta interface energy and average per-residue side-chain

521 RMSD metrics for interface residue rotamer positions. **b**. Average per-residue side chain RMSD

522 for interface helix residues of CVD293 and CVD432 **c-d.** Superposition of critical interface

523 residues of the top 80 selected cryo-EM based models for CVD293 and CVD432. **e**. Average

524 Rosetta interface energy for CVD293 design model, CVD293 cryo-EM based models, CVD432

525 design model and CVD432 cryo-EM based models.

526

527

528   Figure 4.

529
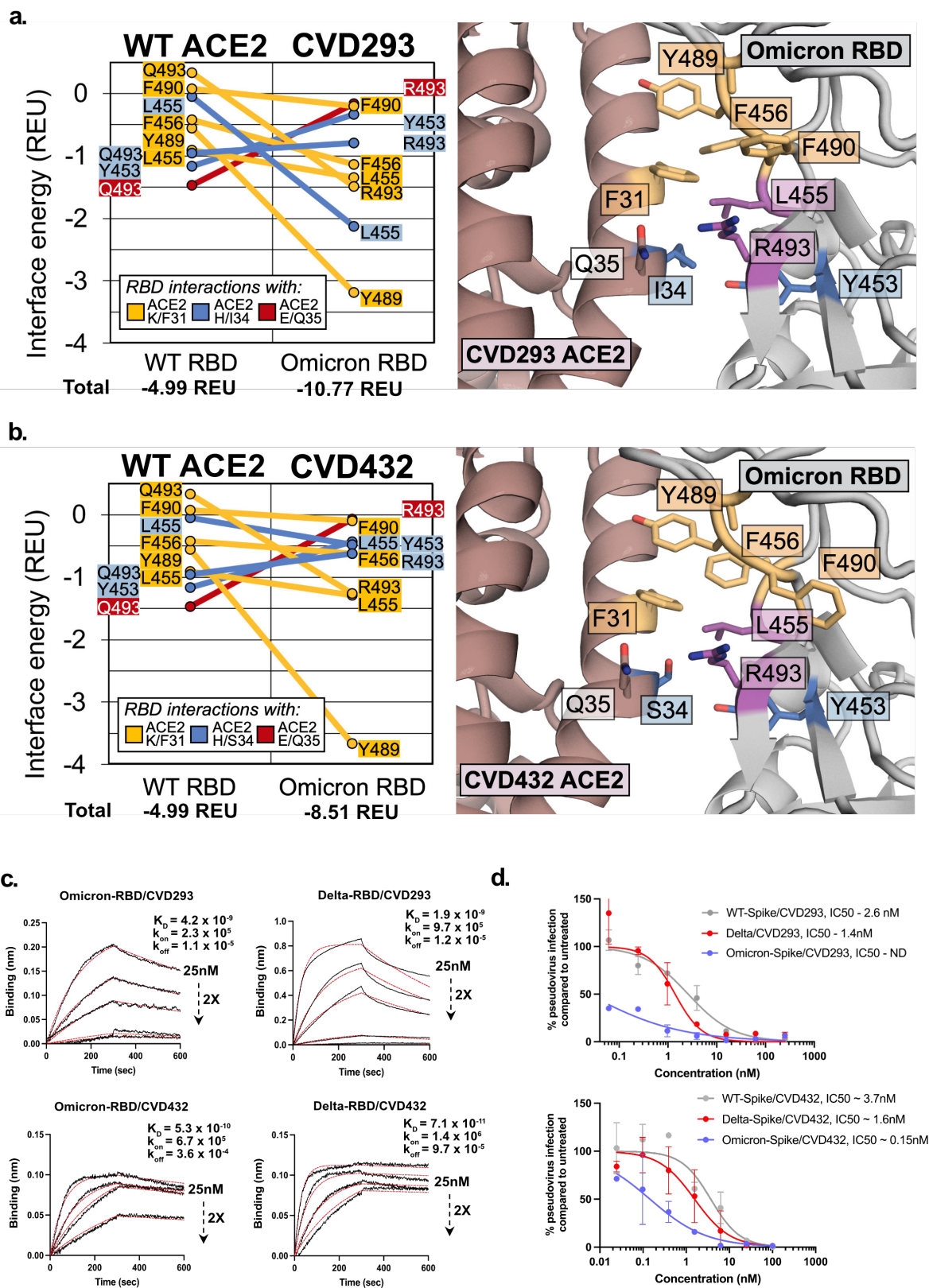
530 **Figure 4. Binding to Omicron- and Delta-RBD and neutralization of Omicron- and Delta-**

531 **SARS-CoV-2 VOCs by CVD293 and CVD432**

532 **a-b.** Left panel - Predictions based on Rosetta interface energy calculations suggest that

533 Omicron-RBD binds CVD293 and CVD432 with high affinity. Residue pair interactions of RBD

534 residues with CVD293/CVD432 residue F31 (yellow), with residue I34/S34 (blue) and with residue

535 Q35 (red) are shown. Right panel - Zoomed in view of the interface of the models Omicron-

536 RBD/CVD293 and Omicron-RBD/CVD432. Wheat-colored residues indicate RBD interactions

537 ACE2 K/F31. Blue residues indicate RBD interactions with ACE2 H/I/S34. Magenta residues

538 indicate RBD interactions with more than one engineered ACE2 residue **c.** Biolayer interferometry

539 measurements for CVD293 or CVD432 interactions with Omicron- or Delta-RBD. **d.** CVD293 and

540 CVD432 potently neutralize vesicular stomatitis virus (VSV) pseudotyped with SARS-CoV2

541 Omicron- and Delta-Spike. Error bars represent standard deviation over all technical replicates

542 from two biological replicates.

543

544

Materials and Methods

Cloning, Expression and Purification of Protein Constructs

WT-fl-Spike plasmid was a generous gift from the Pak lab (Chan Zuckerberg Initiative Biohub) and Krammer lab (Icahn School of Medicine at Mount Sinai). WT-fl-Spike construct has an N-terminal spike protein signal peptide, a trimerization domain and C-terminal 6XHis-tag. WT, Delta-, Omicron-SARS-CoV-2 spike RBD and ACE2 variants (CVD293) were cloned into a pFUSE-based vector with Zeocin antibiotic resistance marker for mammalian expression using the Gibson method. The SARS-CoV-2 spike RBD construct has an IL2 secretion signal followed by the gene of interest, a Gly-Ser linker, a TEV protease cut site, a Gly-Ser linker, an 8X His-tag and an Avitag. CVD293 was cloned into a similar construct with N-terminal IL2 secretion signal followed by ACE2 with the relevant mutations (K31F, H34I, E35Q), a Gly-Ser linker, a TEV protease cut site, a Gly-Ser linker, a human IgG1 hinge and Fc, and AviTag. Construct CVD432 was purchased from Twist Bioscience (www.twistbioscience.com). The construct has an Ampicillin resistance marker, an N-terminal ACE2 secretion signal followed by ACE2 with the relevant CVD313 mutations (K31F, N33D, H34S, E35Q), a short Gly-Ser linker, a human IgG1 hinge and Fc. Also, the H345L mutation in CVD313 was reverted to wildtype residue, histidine.

WT-fl-Spike protein was purified based on the previously described protocol (Weinberg et al., 2021) 30ml of ExpiCHO-S cells at 6M cells/mL were transfected with 1ug/mL of the spike WT using the ExpiCHO™ Expression System Kit (Gibco, catalog # A29133) following the manufacturer's Standard protocol. Briefly, the transfected cells were shaken at 37°C and 8% CO_2 and 18 hours post-transfection, the cultures were supplemented with ExpiCHO™ Feed and ExpiFectamine™ CHO Enhancer and continued to be shaken at 37°C and 8% CO_2 for up to 10 days. The supernatant with secreted spike protein was collected by centrifugation of the culture at 4000xG for 15 mins. The media was filtered using a 0.42μM filter and was transferred to a 50

571   mL centrifuge tube. The sample was then mixed with 2 mL washed Ni-Excel resin (Millipore

572   Sigma, catalog # GE17371201) pre-equilibrated with 10 mM Tris/HCl, pH 8.0, 200 mM NaCl and

573   placed on a rocker for 1 hour at room temperature. After binding, the sample was washed with 25

574   bed volumes of Wash buffer (10 mM Tris/HCl, pH 8.0, 200 mM NaCl, 10 mM imidazole), and

575   eluted with 7 bed volumes of elution buffer (10 mM Tris pH 8.0, 200 mM NaCl, 500 mM imidazole)

576   into separate 2 mL centrifuge tubes. The eluent was concentrated, filtered, and a final SEC

577   polishing step was performed on Superose® 6 10/300 Increase (Millipore Sigma, catalog # GE17-

578   5172-01) pre-equilibrated in 10 mM HEPES pH 8.0, 200 mM NaCl at 4ºC.

579

580   WT, Delta-, Omicron-SARS-CoV-2 spike RBD and ACE2 variants (CVD293 and CVD432) were

581   expressed in high density Expi293F™ cells in Expi293™ expression media following

582   manufacturer's protocol (Expi293 Expression System, ThermoFisher Scientific). Briefly, 3×10^6

583   cell/ml at >95% viability in 25ml media were transfected with ~30ug of DNA using

584   ExpiFectamine™ transfection reagent and Opti-MEM™ I medium. The transfected cells were

585   incubated at 37 °C, 8% CO_2 on an orbital shaker, supplemented with ExpiFectamine™ 293

586   Transfection Enhancer 1 and ExpiFectamine™ 293 Transfection Enhancer 2 about 18-22 hours

587   post-transfection and continued to be incubated at 37 °C, 8% CO_2 on an orbital shaker for

588   additional 4-5 days. Cells were harvested 4-5 days post-transfection, centrifuged at 3000 x g for

589   15 minutes, supernatant collected and filtered through 0.22µM syringe filter. Proteins were

590   neutralized with 10X phosphate buffered saline (PBS, 0.01 M phosphate buffer, 0.0027 M KCl

591   and 0.137 M NaCl, Millipore Sigma P4417-100TAB), pH 7.4 to a final concentration of 2.5x PBS

592   (342.5 mM NaCl, 6.75 mM KCl and 29.75 mM phosphates). SARS-CoV-2 RBDs were purified

593   using cobalt-based immobilized metal affinity chromatography followed by buffer exchange into

594   1X PBS using a Superdex 200 Increase 10/300 GL column (Cytiva). Fc-fused ACE2 proteins

595   were purified on HiTrap Protein A column (GE Healthcare) and eluted with 50 mM Tris pH 7.2, 4

596   M $MgCl_2$ and buffer exchanged into 1X PBS. The protein concentrations were estimated based

597 on the protein absorbance at 280 nm with a spectrophotometer (Nanodrop One, Thermo).

598 All the proteins were >95% pure as determined by SDS-Page gel electrophoresis. The proteins

599 were aliquoted, flash frozen, and stored in -80°C.

600

601 **Cryo-electron Microscopy Sample Preparation and Data Collection -** Purified WT-fl-Spike at

602 2 µM was mixed with either CVD293 (at 2.5 µM) or CVD432 (at 3 µM) just prior to plunge freezing.

603 300 mesh 1.2/1.3R UltrAufoil grids were glow discharged at 15 mA for 30 seconds. Vitrification

604 was done using FEI Vitrobot Mark IV (ThermoFisher) set up at 4°C and 100% humidity. 4 µl

605 complex sample was applied to the grids and the blotting was performed with a blot force of 0 for

606 4 s prior to plunge freezing into liquid ethane. For WT-fl-Spike/CVD293 complex, two datasets

607 comprising of 2,058 and 3,636 120-frame super-resolution movies each were collected while for

608 WT-fl-Spike/CVD432 complex, three datasets comprising of 4,915, 3,196, and 2,574 120-frame

609 super-resolution movies each were collected. For both complexes movies were acquired in super-

610 resolution mode on a Titan Krios (ThermoFisher) equipped with a K3 camera and a Bioquantum

611 energy filter (Gatan) set to a slit width of 20 eV. Collection was performed with a 3x3 image shift

612 at a calibrated magnification of 105, 000 x corresponding to a super resolution pixel size of 0.4265

613 Å/pix. Collection dose rate was 8 e$^-$/physical pixel/second for a total dose of 68 e$^-$/Å$_2$. Defocus

614 range was -0.8 to -1.8 µm. Movies were subsequently corrected for drift using MotionCor2 (Zheng

615 et al., 2017) and were Fourier-cropped by a factor of 2 to a final pixel size of 0.834 Å/pixel. Each

616 collection was performed with semi-automated scripts in SerialEM (Mastronarde, 2003, 2005).

617

618 **Data Processing -**

619

620 **WT-fl-Spike/CVD293 complex 1-RBD-up state (**Figure S2**):** Initial processing was done in

621 cryoSPARC (v2.15.0) (Punjani et al., 2017, 2020). The two datasets with 3636 and 2058 dose-

622 weighted motion corrected micrographs (Zheng et al., 2017) were imported and Patch CTF(M)

623 was performed. Micrographs were curated based on CTF-fit resolution (<4 Å), ice-thickness, and

624 presence of carbon. After manual curation, 3144 and 1575 micrographs were selected for further

625 processing. Blob-picker was used to pick 1,673,305 and 831,773 particles and extraction was

626 done with a box size of 580 px downsized to 480 px for each dataset. 2D-classification was done

627 into 150 classes and good classes were selected with a total of 401,671 particles combined from

628 both datasets. Multiple rounds of heterogeneous, homogenous, and non-uniform refinements in

629 cryoSPARC and focused classification in cisTEM (Grant et al., 2018) resulted in a 3.77 Å 3D-

630 reconstruction of WT-fl-Spike/CVD293 with 61,033 particles. Particle subtraction/local refinement

631 was performed on this final stack of particles focusing on the CVD293/RBD to obtain a 3.50 Å 3D

632 reconstruction of WT-Spike-RBD (residues 331-541)/CVD293 (residues 18-614).

633

634 **WT-fl-Spike/CVD432 complex 1-RBD-up state (**Figure S3**):** Initial processing was done in

635 cryoSPARC (v2.15.0). The three datasets with 4915, 3916 and 2574 dose-weighted motion

636 corrected micrographs were imported and Patch CTF(M) was performed. Micrographs were

637 curated based on CTF-fit resolution (<4 Å), ice-thickness, and presence of carbon. After manual

638 curation, 3864, 2238 and 2148 micrographs were selected for further processing. Blob-picker was

639 used to pick 1,259,441 particles from Dataset 1 while template-based particle picker (260 Å

640 diameter) was used to pick 782,620 and 752,648 particles for Dataset 2 and Dataset 3,

641 respectively. Extraction was done with a box size of 512 px for Dataset 1 which was re-extracted

642 with box size of 600 px after a round of ab-initio refinement and finally downsampled to 400 px.

643 For Datasets 2 and 3, extraction was done at box size 600 px and then downsampled to 400 px.

644 2D-classification was done with 150 classes for each dataset and good classes of WT-fl-

645 Spike/CVD432 in 1-RBD-up state were selected with a total of 601,624 particles combined from

646 the three datasets. Multiple rounds of heterogeneous, non-uniform refinements and homogenous

647 refinements in cryoSPARC and focused classification in cisTEM resulted in a 3.5 Å 3D-

648 reconstruction of WT-fl-Spike/CVD432 1-RBD-up state with 97,082 particles. Particle

649 subtraction/local refinement was performed on this final stack of particles focusing on the

650 CVD432/RBD to obtain a 3.36 Å 3D reconstruction of WT-Spike-RBD (residues 331-

651 541)/CVD432 (residues 18-614).

652

653 **WT-fl-Spike/CVD432 complex 2-RBD-up state (**Figure S4**):** We processed the WT-fl-

654 Spike/CVD432 complex 2-RBD-up state independent of the 1-RBD-up state**.** Initial processing

655 was done in cryoSPARC (v2.15.0). The three datasets with 4915, 3916 and 2574 dose-weighted

656 motion corrected micrographs were imported and Patch CTF(M) was performed. Micrographs

657 were curated based on CTF-fit resolution (<4 Å), ice-thickness, and presence of carbon. After

658 manual curation, 3833, 2253 and 2175 micrographs were selected for further processing. We first

659 used blob-picker on Dataset 1 to pick 1,597,143 and after 2D classification, 19 good classes were

660 selected. The 19 classes from Data set 1 were used for template-based particle picker (220 Å

661 diameter) to pick 1,499,401 and 1,019,564 and 1,328,287 particles for Dataset 1, Dataset 2 and

662 Dataset 3, respectively. Extraction was done at box size 600 px for all datasets. 2D-classification

663 was done into 150 classes for each dataset and good looking classes with WT-fl-Spike/CVD432

664 in 2-RBD-up state were selected with a total of 113,836 particles combined from the three

665 datasets. Multiple rounds of heterogeneous, non-uniform refinements and homogenous

666 refinements in cryoSPARC and focused classification in cisTEM resulted in a 2.97 Å 3D-

667 reconstruction of WT-fl-Spike/CVD432 2-up state with 97,374 particles. Each WT-Spike-

668 RBD/CVD432 interface in the 2-RBD-up state was at an overall low resolution and particle

669 subtraction/local refinement was not performed.

670

671

672 **Model Building and Refinement -**

673

674 ***Low resolution rigid body fitting***

675

676 1-RBD-up state WT-fl-Spike/WT-ACE2 model with PDB ID - 7DX5, was used as the initial model

677 for rigid body fitting into cryo-EM density map of 1-RBD-up state of WT-fl-Spike/CVD293 or 1-

678 RBD-up state of WT-fl-Spike/CVD432 in CHIMERA (Pettersen et al., 2004). For 2-RBD-up state

679 of WT-fl-Spike/CVD432, we generated a model by rigid body fitting PDB ID - 7DX5 into the density

680 map and simultaneously rigid body fitting WT-Spike-RBD/ACE2 (18-614) complex with PDB ID -

681 6M0J into the second RBD-up region of the map in CHIMERA. The final model was fit using

682 FastRelax in torsion space in Rosetta into the WT-fl-Spike/WT-ACE2 2-RBD-up state cryo-EM

683 map. Rosetta into the Overall, the fits agree with previously reported 1-RBD-up states for WT-fl-

684 Spike/ACE2 (18-614) complexes.

685

686 **High resolution "final consensus" model building**

687

688 High resolution map of WT-Spike-RBD/CVD293 (18-614) with mutations K31F, H34I, E35Q or

689 WT-Spike-RBD/CVD432 (18-614) with mutations K31F, N33D, H34S, E35Q were generated from

690 WT-fl-Spike/CVD293 map or WT-fl-Spike/CVD432 map, respectively, in cryoSPARC (v2.15.0) by

691 Particle subtraction/Local refinement. PDB ID: 6M0J was used for initial rigid body fit into the WT-

692 Spike-RBD/CVD293 (18-614) map. This model was then refined against the respective maps in

693 Phenix Real Space Refine (Liebschner et al., 2019) with the corrected sequence input for CVD293

694 or CVD432. This was followed by a FastRelax in torsion space with Rosetta (2020.08 release)

695 (Wang et al., 2016). Model for each complex was manually examined and corrected using COOT

696 0.9 (Emsley et al., 2010) and ISOLDE 1.0 (Croll, 2018). The B-factors were assigned using a

697 Rosetta B-factor fitting mover. Local resolution was determined by running the ResMap program

698 (Kucukelbir et al., 2014). Directional FSC curves were determined by submitting the associated

699 files to the 3DFSC server (Tan et al., 2017). Q-scores were calculated using the Q-score plugin

700 for USCF Chimera (Pintilie et al., 2020).

701

Multi-model Pipeline

703

704   The Cryo-EM consensus model of WT-Spike-RBD/CVD293 (18-614) or WT-Spike-RBD/CVD432

705   (18-614) was used as the starting model for the pipeline. We applied the Rosetta Iterative Rebuild

706   protocol on 10-amino acid overlapping stretches of the interface helix for each consensus model.

707   The parameters used were defined in an XML file (Parameters.xml) found in SI Appendix:

708   Supplemental computational methods: Commands and input files section. For each 10-amino

709   acid stretch of the interface helix we generated 2000 independent models totaling 8000 models

710   for the entire interface helix from ACE2 residue 21 to residue 52. Total of 200 models were then

711   selected based on the total Rosetta energy score followed by the top 20 that best fit to the map

712   destiny. A total of 80 top selected models for each complex were then used for further analyses.

713   We calculated the local average per residue average side-chain RMSD in CHIMERA and average

714   interface energy (in REU) for the residues of the interface helix.

715

Energy calculations

717

718   Total and individual pairwise interface energies were calculated for all design models and cryo-

719   EM atomic models using the Rosetta interface energy application. Per-residue energies were

720   calculated using the Rosetta per-residue energy application, and total energies were calculated

721   using the Rosetta scoring application in Rosetta

722   (2021.48.post.dev+8.master.77491fa20be77491fa20be83588cfc37ab422ba5b95eca128ebgit@

723   github.com:RosettaCommons/main.git 2021-12-02T08:56:13) (Alford et al., 2017; Leman et al.,

724   2020) . For the cryo-EM atomic models of CVD293 and CVD432, all scores were averaged and

725   standard deviations were calculated. The command lines and code are available in the *SI*

726   *Appendix: Supplemental computational methods: Commands and input files section.*

727

Design models of the ACE2 domain of CVD432

729

730 Design models of the ACE2 domain of CVD432 were generated using the RosettaScripts

731 framework (Glasgow et al., 2020). Beginning with the atomic models of CVD293 solved by cryo-

732 EM using the multi-model pipeline, we mutated N33 and I34 to aspartic acid and serine,

733 respectively, in each of the 80 WT-Spike-RBD/CVD293 cryo-EM based models and minimized

734 the complexes. Total energies and interface energies were calculated as described in "Energy

735 calculations." The average interface energies and standard deviation is shown as CVD293 cryo-

736 EM based models in Figure 3e. The code is available in the *SI Appendix: Supplemental*

737 *computational methods: Commands and input files section.*

738

Determination of binding affinity using biolayer interferometry (BLI)

740

741 Affinity measurements were carried out at room temperature using an Octet RED384 system. In

742 our BLI experiments, ACE2 Fc-fusions are tethered to either Streptavidin biosensors (WT-ACE2,

743 CVD293) (Sartorius®, Item no.: 18-5019) or ProtA biosensors (Sartorius®, Item no.: 18-5010)

744 and WT, Delta-, Omicron-SARS-CoV-2 spike RBD are present as the analyte in solution in a 384-

745 well microplate. The biosensors were washed in phosphate buffered saline (1X PBS) with 0.05%

746 Tween-20 at pH 7.4 and 0.2% bovine serum albumin (BSA) (1X PBSTB) for 200 seconds.

747 Antigens WT-ACE2, CVD293 were diluted to 10 nM in 1X PBSTB containing 10 μM biotin (1X

748 PBSTBB) as blocking agent while antigen CVD432 was diluted 10nM in 1X PBSTB. The antigens

749 were then loaded to the respective biosensors for 300 seconds. Following loading, a baseline was

750 established by washing the WT-ACE2 or CVD293 bound Streptavidin biosensors in 1X PBSTBB

751 and CVD432 bound ProtA biosensors in 1X PBSTB for 200 seconds. WT, Delta-, Omicron-SARS-

752 CoV-2 spike RBD were then allowed to associate with the antigen at concentrations ranging from

753 0 to 25 nM of Spike for about 600 seconds and then returned to the respective washing well to

754 follow dissociation for about 900 seconds. Raw data were fit in Octet Data Analysis HT software

755 version 10.0 using curve-fitting kinetic analysis with global fitting and assuming 1:1 non-

756 cooperative binding kinetics. All fits to BLI data had R^2 (goodness of fit) > 0.90.

757

Pseudovirus Production

759 SARS-CoV-2 pseudoviruses bearing spike proteins of variants of interest were generated as

760 previously described (Hoffmann et al., 2020; Laurie et al., 2021, 2022) using a recombinant

761 vesicular stomatitis virus (VSV) expressing green fluorescent protein (GFP) in place of the VSV

762 glycoprotein (rVSV Δ G-GFP). B.1 (WT, 1 spike mutation (D614G)), B.1.617.2/delta (9-10 spike

763 mutations), and B.1.1.529/ omicron (37 spike mutations) were cloned in a cytomegalovirus

764 enhancer-driven expression vector and used to produce SARS-CoV-2 spike pseudoviruses. The

765 mutations for each variant are listed as follows - B.1/WT (D614G), B.1.617.2/Delta (T19R, T95I,

766 G142D, Δ157-158, L452R, T478K, P681R, D614G, D950N), B.1.1.529/Omicron (A67V, ΔH69,

767 ΔV70, T95I, ΔG142, ΔV143, ΔY144, Y145D, ΔN211, L212I, G339D, S371L, S373P, S375F,

768 K417N, N440K, G446S, S477N, T478K, E484A, Q493R, G496S, Q498R, N501Y, Y505H, T547K,

769 D614G, H655Y, N679K, P681H, N764K, D796Y, N856K, Q954H, N969K, L981F). Pseudoviruses

770 were titered on Huh7.5.1 cells overexpressing ACE2 and TMPRSS2 (gift of Andreas Puschnik)

771 using GFP expression to measure the concentration of focus forming units (ffu).

Pseudovirus Neutralization Assay

773

774 Pseudovirus Neutralization Assay was performed as described previously (Laurie et al., 2021,

775 2022) Huh7.5.1-ACE2-TMPRSS2 cells were seeded in 96-well plates at a density of 7000-8000

776 cells/well 1 day prior to pseudovirus infection. ACE2 receptor traps were serially diluted into

777 complete culture media (Dulbecco's Modified Eagle's Medium with 10% fetal bovine serum,

778   10mM HEPES, 1X Pen-Strep-Glutamine). Each pseudovirus was diluted to 125 ffu/µL and 30 µL

779   of each pseudovirus was mixed with ~30 µL of ACE2 receptor traps or media only. Media only

780   with no pseudovirus served as an additional control. These were incubated at 37°C for 1 hour

781   before adding 50 µL of virus:binder incubated mix directly to previously plated cells. Cells

782   inoculated with ACE2 receptor traps/pseudovirus mixtures were incubated at 37°C and 5% CO_2

783   for 24 hours. The cells were then lifted and resuspended using 20 µL of 10X TrypLE Select (Gibco)

784   and GFP signal of infected cells recorded using Beckman CytoFlex Cytometer B4R3V4.

785   Data were analyzed with FlowJo[TM] to determine percent GFP-positive pseudovirus transduced

786   cells. GFP-signals from wells with no ACE2 receptor traps (media only with pseudovirus) were

787   used to normalize the data and determine percent neutralization. A 7-8 point dose-response curve

788   was generated in GraphPad Prism and IC50s reported in µg/mL. The reported IC50s are based

789   on two technical and biological replicates for each pseudovirus/ACE2 receptor trap pair.

790

Bibliography

Alford, R.F., Leaver-Fay, A., Jeliazkov, J.R., O'Meara, M.J., DiMaio, F.P., Park, H., Shapovalov, M.V., Renfrew, P.D., Mulligan, V.K., Kappel, K., et al. (2017). The Rosetta All-Atom Energy Function for Macromolecular Modeling and Design. J. Chem. Theory Comput. *13*, 3031–3048. https://doi.org/10.1021/acs.jctc.7b00125.

Barnes, C.O., West, A.P., Huey-Tubman, K.E., Hoffmann, M.A.G., Sharaf, N.G., Hoffman, P.R., Koranda, N., Gristick, H.B., Gaebler, C., Muecksch, F., et al. (2020a). Structures of Human Antibodies Bound to SARS-CoV-2 Spike Reveal Common Epitopes and Recurrent Features of Antibodies. Cell *182*, 828-842.e16. https://doi.org/10.1016/j.cell.2020.06.025.

Barnes, C.O., Jette, C.A., Abernathy, M.E., Dam, K.-M.A., Esswein, S.R., Gristick, H.B., Malyutin, A.G., Sharaf, N.G., Huey-Tubman, K.E., Lee, Y.E., et al. (2020b). SARS-CoV-2 neutralizing antibody structures inform therapeutic strategies. Nature *588*, 682–687. https://doi.org/10.1038/s41586-020-2852-1.

Barton, M.I., MacGowan, S.A., Kutuzov, M.A., Dushek, O., Barton, G.J., and van der Merwe, P.A. (2021). Effects of common mutations in the SARS-CoV-2 Spike RBD and its ligand, the human ACE2 receptor on binding affinity and kinetics. ELife *10*. https://doi.org/10.7554/eLife.70658.

Baum, A., Fulton, B.O., Wloga, E., Copin, R., Pascal, K.E., Russo, V., Giordano, S., Lanza, K., Negron, N., Ni, M., et al. (2020). Antibody cocktail to SARS-CoV-2 spike protein prevents rapid mutational escape seen with individual antibodies. Science *369*, 1014–1018. https://doi.org/10.1126/science.abd0831.

Cameroni, E., Bowen, J.E., Rosen, L.E., Saliba, C., Zepeda, S.K., Culap, K., Pinto, D., VanBlargan, L.A., De Marco, A., di Iulio, J., et al. (2022). Broadly neutralizing antibodies overcome SARS-CoV-2 Omicron antigenic shift. Nature *602*, 664–670.

815   https://doi.org/10.1038/s41586-021-04386-2.

816   Cao, Y., Wang, J., Jian, F., Xiao, T., Song, W., Yisimayi, A., Huang, W., Li, Q., Wang, P., An,

817   R., et al. (2022). Omicron escapes the majority of existing SARS-CoV-2 neutralizing antibodies.

818   Nature *602*, 657–663. https://doi.org/10.1038/s41586-021-04385-3.

819   Cele, S., Jackson, L., Khoury, D.S., Khan, K., Moyo-Gwete, T., Tegally, H., San, J.E., Cromer,

820   D., Scheepers, C., Amoako, D., et al. (2021). SARS-CoV-2 Omicron has extensive but

821   incomplete escape of Pfizer BNT162b2 elicited neutralization and requires ACE2 for infection.

822   MedRxiv https://doi.org/10.1101/2021.12.08.21267417.

823   Chan, K.K., Dorosky, D., Sharma, P., Abbasi, S.A., Dye, J.M., Kranz, D.M., Herbert, A.S., and

824   Procko, E. (2020). Engineering human ACE2 to optimize binding to the spike protein of SARS

825   coronavirus 2. Science *369*, 1261–1265. https://doi.org/10.1126/science.abc0870.

826   Chowdhury, R., Boorla, V.S., Maranas, C.D. (2020). Computational biophysical characterization

827   of the SARS-CoV-2 spike protein binding with the ACE2 receptor and implications for infectivity.

828   Comput Struct Biotechnol J. *18*, 2573-2582.

829   Cohen, M.S., Nirula, A., Mulligan, M.J., Novak, R.M., Marovich, M., Yen, C., Stemer, A., Mayer,

830   S.M., Wohl, D., Brengle, B., et al. (2021). Effect of Bamlanivimab vs Placebo on Incidence of

831   COVID-19 Among Residents and Staff of Skilled Nursing and Assisted Living Facilities: A

832   Randomized Clinical Trial. JAMA *326*, 46–55. https://doi.org/10.1001/jama.2021.8828.

833   Croll, T.I. (2018). ISOLDE: a physically realistic environment for model building into low-

834   resolution electron-density maps. Acta Crystallogr. D Struct. Biol. *74*, 519–530.

835   https://doi.org/10.1107/S2059798318002425.

836   DiMaio, F., Song, Y., Li, X., Brunner, M.J., Xu, C., Conticello, V., Egelman, E., Marlovits, T.,

837   Cheng, Y., and Baker, D. (2015). Atomic-accuracy models from 4.5-Å cryo-electron microscopy

838   data with density-guided iterative local refinement. Nat. Methods *12*, 361–365.

839   https://doi.org/10.1038/nmeth.3286.

840   Dong, J., Zost, S.J., Greaney, A.J., Starr, T.N., Dingens, A.S., Chen, E.C., Chen, R.E., Case,

841   J.B., Sutton, R.E., Gilchuk, P., et al. (2021). Genetic and structural basis for SARS-CoV-2

842   variant neutralization by a two-antibody cocktail. Nat. Microbiol. *6*, 1233–1244.

843   https://doi.org/10.1038/s41564-021-00972-2.

844   Emsley, P., Lohkamp, B., Scott, W.G., and Cowtan, K. (2010). Features and development of

845   Coot. Acta Crystallogr. D Biol. Crystallogr. *66*, 486–501.

846   https://doi.org/10.1107/S0907444910007493.

847   Glasgow, A., Glasgow, J., Limonta, D., Solomon, P., Lui, I., Zhang, Y., Nix, M.A., Rettko, N.J.,

848   Zha, S., Yamin, R., et al. (2020). Engineered ACE2 receptor traps potently neutralize SARS-

849   CoV-2. Proc Natl Acad Sci USA *117*, 28046–28055. https://doi.org/10.1073/pnas.2016093117.

850   Gottlieb, R.L., Nirula, A., Chen, P., Boscia, J., Heller, B., Morris, J., Huhn, G., Cardona, J.,

851   Mocherla, B., Stosor, V., et al. (2021). Effect of Bamlanivimab as Monotherapy or in

852   Combination With Etesevimab on Viral Load in Patients With Mild to Moderate COVID-19: A

853   Randomized Clinical Trial. JAMA *325*, 632–644. https://doi.org/10.1001/jama.2021.0202.

854   Grant, T., Rohou, A., and Grigorieff, N. (2018). cisTEM, user-friendly software for single-particle

855   image processing. ELife *7*, e35383. https://doi.org/10.7554/eLife.35383.

856   Hansen, J., Baum, A., Pascal, K.E., Russo, V., Giordano, S., Wloga, E., Fulton, B.O., Yan, Y.,

857   Koon, K., Patel, K., et al. (2020). Studies in humanized mice and convalescent humans yield a

858   SARS-CoV-2 antibody cocktail. Science *369*, 1010–1014.

859   https://doi.org/10.1126/science.abd0827.

860   Herzik, M.A., Fraser, J.S., and Lander, G.C. (2019). A Multi-model Approach to Assessing Local

861   and Global Cryo-EM Map Quality. Structure *27*, 344-358.e3.

862   https://doi.org/10.1016/j.str.2018.10.003.

863 Higuchi, Y., Suzuki, T., Arimori, T., Ikemura, N., Mihara, E., Kirita, Y., Ohgitani, E., Mazda, O.,

864 Motooka, D., Nakamura, S., et al. (2021). Engineered ACE2 receptor therapy overcomes

865 mutational escape of SARS-CoV-2. Nat. Commun. *12*, 3802. https://doi.org/10.1038/s41467-

866 021-24013-y.

867 Hoffmann, M., Kleine-Weber, H., and Pöhlmann, S. (2020). A Multibasic Cleavage Site in the

868 Spike Protein of SARS-CoV-2 Is Essential for Infection of Human Lung Cells. Mol. Cell *78*, 779-

869 784.e5. https://doi.org/10.1016/j.molcel.2020.04.022.

870 Ikemura, N., Taminishi, S., Inaba, T., Arimori, T., Motooka, D., Katoh, K., Kirita, Y., Higuchi, Y.,

871 Li, S., Itoh, Y., et al. (2021). Engineered ACE2 counteracts vaccine-evading SARS-CoV-2

872 Omicron variant. BioRxiv https://doi.org/10.1101/2021.12.22.473804.

873 Jones, B.E., Brown-Augsburger, P.L., Corbett, K.S., Westendorf, K., Davies, J., Cujec, T.P.,

874 Wiethoff, C.M., Blackbourne, J.L., Heinz, B.A., Foster, D., et al. (2021). The neutralizing

875 antibody, LY-CoV555, protects against SARS-CoV-2 infection in nonhuman primates. Sci.

876 Transl. Med. *13*. https://doi.org/10.1126/scitranslmed.abf1906.

877 Koerber, J.T., Thomsen, N.D., Hannigan, B.T., Degrado, W.F., and Wells, J.A. (2013). Nature-

878 inspired design of motif-specific antibody scaffolds. Nat. Biotechnol. *31*, 916–921.

879 https://doi.org/10.1038/nbt.2672.

880 Kucukelbir, A., Sigworth, F.J., and Tagare, H.D. (2014). Quantifying the local resolution of cryo-

881 EM density maps. Nat. Methods *11*, 63–65. https://doi.org/10.1038/nmeth.2727.

882 Laffeber, C., de Koning, K., Kanaar, R., and Lebbink, J.H.G. (2021). Experimental Evidence for

883 Enhanced Receptor Binding by Rapidly Spreading SARS-CoV-2 Variants. J. Mol. Biol. *433*,

884 167058. https://doi.org/10.1016/j.jmb.2021.167058.

885 Laurie, M.T., Liu, J., Sunshine, S., Peng, J., Black, D., Mitchell, A.M., Mann, S.A., Pilarowski,

886 G., Zorn, K.C., Rubio, L., et al. (2021). SARS-CoV-2 variant exposures elicit antibody responses

887   with differential cross-neutralization of established and emerging strains including Delta and

888   Omicron. MedRxiv https://doi.org/10.1101/2021.09.08.21263095.

889   Laurie, M.T., Liu, J., Sunshine, S., Peng, J., Black, D., Mitchell, A.M., Mann, S.A., Pilarowski,

890   G., Zorn, K.C., Rubio, L., et al. (2022). SARS-CoV-2 Variant Exposures Elicit Antibody

891   Responses With Differential Cross-Neutralization of Established and Emerging Strains Including

892   Delta and Omicron. J. Infect. Dis. *225*, 1909–1914. https://doi.org/10.1093/infdis/jiab635.

893   Lei, C., Qian, K., Li, T., Zhang, S., Fu, W., Ding, M., and Hu, S. (2020). Neutralization of SARS-

894   CoV-2 spike pseudotyped virus by recombinant ACE2-Ig. Nat. Commun. *11*, 2070.

895   https://doi.org/10.1038/s41467-020-16048-4.

896   Leman, J.K., Weitzner, B.D., Lewis, S.M., Adolf-Bryfogle, J., Alam, N., Alford, R.F., Aprahamian,

897   M., Baker, D., Barlow, K.A., Barth, P., et al. (2020). Macromolecular modeling and design in

898   Rosetta: recent methods and frameworks. Nat. Methods *17*, 665–680.

899   https://doi.org/10.1038/s41592-020-0848-2.

900   Liebschner, D., Afonine, P.V., Baker, M.L., Bunkóczi, G., Chen, V.B., Croll, T.I., Hintze, B.,

901   Hung, L.W., Jain, S., McCoy, A.J., et al. (2019). Macromolecular structure determination using

902   X-rays, neutrons and electrons: recent developments in Phenix. Acta Crystallogr. D Struct. Biol.

903   *75*, 861–877. https://doi.org/10.1107/S2059798319011471.

904   Liu, H., Zhang, Q., Wei, P., Chen, Z., Aviszus, K., Yang, J., Downing, W., Jiang, C., Liang, B.,

905   Reynoso, L., et al. (2021). The basis of a more contagious 501Y.V1 variant of SARS-CoV-2.

906   Cell Res. *31*, 720–722. https://doi.org/10.1038/s41422-021-00496-8.

907   Liu, L., Wang, P., Nair, M.S., Yu, J., Rapp, M., Wang, Q., Luo, Y., Chan, J.F.-W., Sahi, V.,

908   Figueroa, A., et al. (2020). Potent neutralizing antibodies against multiple epitopes on SARS-

909   CoV-2 spike. Nature *584*, 450–456. https://doi.org/10.1038/s41586-020-2571-7.

910   Liu, L., Iketani, S., Guo, Y., Chan, J.F.-W., Wang, M., Liu, L., Luo, Y., Chu, H., Huang, Y., Nair,

911   M.S., et al. (2022). Striking antibody evasion manifested by the Omicron variant of SARS-CoV-

912   2. Nature *602*, 676–681. https://doi.org/10.1038/s41586-021-04388-0.

913   Mannar, D., Saville, J.W., Zhu, X., Srivastava, S.S., Berezuk, A.M., Zhou, S., Tuttle, K.S., Kim,

914   A., Li, W., Dimitrov, D.S., et al. (2021). Structural analysis of receptor binding domain mutations

915   in SARS-CoV-2 variants of concern that modulate ACE2 and antibody binding. Cell Rep. *37*,

916   110156. https://doi.org/10.1016/j.celrep.2021.110156.

917   Mannar, D., Saville, J.W., Zhu, X., Srivastava, S.S., Berezuk, A.M., Tuttle, K.S., Marquez, A.C.,

918   Sekirov, I., and Subramaniam, S. (2022). SARS-CoV-2 Omicron variant: Antibody evasion and

919   cryo-EM structure of spike protein-ACE2 complex. Science *375*, 760–764.

920   https://doi.org/10.1126/science.abn7760.

921   Mastronarde, D.N. (2003). Serialem: A program for automated tilt series acquisition on tecnai

922   microscopes using prediction of specimen position. Microsc. Microanal. *9*, 1182–1183.

923   https://doi.org/10.1017/S1431927603445911.

924   Mastronarde, D.N. (2005). Automated electron microscope tomography using robust prediction

925   of specimen movements. J. Struct. Biol. *152*, 36–51. https://doi.org/10.1016/j.jsb.2005.07.007.

926   McCallum, M., Walls, A.C., Sprouse, K.R., Bowen, J.E., Rosen, L.E., Dang, H.V., De Marco, A.,

927   Franko, N., Tilles, S.W., Logue, J., et al. (2021). Molecular basis of immune evasion by the

928   Delta and Kappa SARS-CoV-2 variants. Science *374*, 1621–1626.

929   https://doi.org/10.1126/science.abl8506.

930   McCallum, M., Czudnochowski, N., Rosen, L.E., Zepeda, S.K., Bowen, J.E., Walls, A.C.,

931   Hauser, K., Joshi, A., Stewart, C., Dillen, J.R., et al. (2022). Structural basis of SARS-CoV-2

932   Omicron immune evasion and receptor engagement. Science *375*, 864–868.

933   https://doi.org/10.1126/science.abn8652.

934   Mlcochova, P., Kemp, S.A., Dhar, M.S., Papa, G., Meng, B., Ferreira, I.A.T.M., Datir, R., Collier,

935   D.A., Albecka, A., Singh, S., et al. (2021). SARS-CoV-2 B.1.617.2 Delta variant replication and

936   immune evasion. Nature *599*, 114–119. https://doi.org/10.1038/s41586-021-03944-y.

937   Mou, Y., Zhou, X.X., Leung, K., Martinko, A.J., Yu, J.-Y., Chen, W., and Wells, J.A. (2018).

938   Engineering improved antiphosphotyrosine antibodies based on an immunoconvergent binding

939   motif. J. Am. Chem. Soc. *140*, 16615–16624. https://doi.org/10.1021/jacs.8b08402.

940   Park, Y.-J., De Marco, A., Starr, T.N., Liu, Z., Pinto, D., Walls, A.C., Zatta, F., Zepeda, S.K.,

941   Bowen, J.E., Sprouse, K.R., et al. (2022). Antibody-mediated broad sarbecovirus neutralization

942   through ACE2 molecular mimicry. Science *375*, 449–454.

943   https://doi.org/10.1126/science.abm8143.

944   Pettersen, E.F., Goddard, T.D., Huang, C.C., Couch, G.S., Greenblatt, D.M., Meng, E.C., and

945   Ferrin, T.E. (2004). UCSF Chimera—a visualization system for exploratory research and

946   analysis. J. Comput. Chem. *25*, 1605–1612. https://doi.org/10.1002/jcc.20084.

947   Pintilie, G., Zhang, K., Su, Z., Li, S., Schmid, M.F., and Chiu, W. (2020). Measurement of atom

948   resolvability in cryo-EM maps with Q-scores. Nat. Methods *17*, 328–334.

949   https://doi.org/10.1038/s41592-020-0731-1.

950   Planas, D., Saunders, N., Maes, P., Guivel-Benhassine, F., Planchais, C., Buchrieser, J.,

951   Bolland, W.-H., Porrot, F., Staropoli, I., Lemoine, F., et al. (2022). Considerable escape of

952   SARS-CoV-2 Omicron to antibody neutralization. Nature *602*, 671–675.

953   https://doi.org/10.1038/s41586-021-04389-z.

954   Punjani, A., and Fleet, D.J. (2021). 3D variability analysis: Resolving continuous flexibility and

955   discrete heterogeneity from single particle cryo-EM. J. Struct. Biol. *213*, 107702.

956   https://doi.org/10.1016/j.jsb.2021.107702.

957   Punjani, A., Rubinstein, J.L., Fleet, D.J., and Brubaker, M.A. (2017). cryoSPARC: algorithms for

958   rapid unsupervised cryo-EM structure determination. Nat. Methods *14*, 290–296.

959   https://doi.org/10.1038/nmeth.4169.

960   Punjani, A., Zhang, H., and Fleet, D.J. (2020). Non-uniform refinement: adaptive regularization

961   improves single-particle cryo-EM reconstruction. Nat. Methods *17*, 1214–1221.

962   https://doi.org/10.1038/s41592-020-00990-8.

963   Shi, R., Shan, C., Duan, X., Chen, Z., Liu, P., Song, J., Song, T., Bi, X., Han, C., Wu, L., et al.

964   (2020). A human neutralizing antibody targets the receptor-binding site of SARS-CoV-2. Nature

965   *584*, 120–124. https://doi.org/10.1038/s41586-020-2381-y.

966   Tan, Y.Z., Baldwin, P.R., Davis, J.H., Williamson, J.R., Potter, C.S., Carragher, B., and Lyumkis,

967   D. (2017). Addressing preferred specimen orientation in single-particle cryo-EM through tilting.

968   Nat. Methods *14*, 793–796. https://doi.org/10.1038/nmeth.4347.

969   Tian, F., Tong, B., Sun, L., Shi, S., Zheng, B., Wang, Z., Dong, X., and Zheng, P. (2021). N501Y

970   mutation of spike protein in SARS-CoV-2 strengthens its binding to receptor ACE2. ELife *10*.

971   https://doi.org/10.7554/eLife.69091.

972   Tortorici, M.A., Beltramello, M., Lempp, F.A., Pinto, D., Dang, H.V., Rosen, L.E., McCallum, M.,

973   Bowen, J., Minola, A., Jaconi, S., et al. (2020). Ultrapotent human antibodies protect against

974   SARS-CoV-2 challenge via multiple mechanisms. Science *370*, 950–957.

975   https://doi.org/10.1126/science.abe3354.

976   VanBlargan, L.A., Errico, J.M., Halfmann, P., Zost, S.J., Crowe, J.E., Purcell, L.A., Kawaoka, Y.,

977   Corti, D., Fremont, D.H., and Diamond, M. (2021). An infectious SARS-CoV-2 B.1.1.529

978   Omicron virus escapes neutralization by several therapeutic monoclonal antibodies. BioRxiv

979   https://doi.org/10.1101/2021.12.15.472828.

980   Viana, R., Moyo, S., Amoako, D.G., Tegally, H., Scheepers, C., Althaus, C.L., Anyaneji, U.J.,

981   Bester, P.A., Boni, M.F., Chand, M., et al. (2022). Rapid epidemic expansion of the SARS-CoV-

982   2 Omicron variant in southern Africa. Nature *603*, 679–686. https://doi.org/10.1038/s41586-022-

983   04411-y.

984   Walls, A.C., Park, Y.-J., Tortorici, M.A., Wall, A., McGuire, A.T., and Veesler, D. (2020).

985   Structure, Function, and Antigenicity of the SARS-CoV-2 Spike Glycoprotein. Cell *181*, 281-

986   292.e6. https://doi.org/10.1016/j.cell.2020.02.058.

987   Wang, R.Y.-R., Song, Y., Barad, B.A., Cheng, Y., Fraser, J.S., and DiMaio, F. (2016).

988   Automated structure refinement of macromolecular assemblies from cryo-EM maps using

989   Rosetta. ELife *5*. https://doi.org/10.7554/eLife.17219.

990   Weidenbacher, P.A.-B., Waltari, E., de los Rios Kobara, I., Bell, B.N., Pak, J.E., and Kim, P.S.

991   (2022). Converting non-neutralizing SARS-CoV-2 antibodies targeting conserved epitopes into

992   broad-spectrum inhibitors through receptor blockade. BioRxiv

993   https://doi.org/10.1101/2022.01.24.477625.

994   Weinberg, Z.Y., Hilburger, C.E., Kim, M., Cao, L., Khalid, M., Elmes, S., Diwanji, D., Hernandez,

995   E., Lopez, J., Schaefer, K., et al. (2021). Sentinel cells enable genetic detection of SARS-CoV-2

996   Spike protein. BioRxiv https://doi.org/10.1101/2021.04.20.440678.

997   Wilhelm, A., Widera, M., Grikscheit, K., Toptan, T., Schenk, B., Pallas, C., Metzler, M., Kohmer,

998   N., Hoehl, S., Helfritz, F.A., et al. (2021). Reduced Neutralization of SARS-CoV-2 Omicron

999   Variant by Vaccine Sera and monoclonal antibodies. MedRxiv

1000 https://doi.org/10.1101/2021.12.07.21267432.

1001 Wirnsberger, G., Monteil, V., Eaton, B., Postnikova, E., Murphy, M., Braunsfeld, B., Crozier, I.,

1002 Kricek, F., Niederhöfer, J., Schwarzböck, A., et al. (2021). Clinical grade ACE2 as a universal

1003 agent to block SARS-CoV-2 variants. BioRxiv https://doi.org/10.1101/2021.09.10.459744.

1004 Yan, R., Zhang, Y., Li, Y., Ye, F., Guo, Y., Xia, L., Zhong, X., Chi, X., and Zhou, Q. (2021).

1005 Structural basis for the different states of the spike protein of SARS-CoV-2 in complex with

1006 ACE2. Cell Res. *31*, 717–719. https://doi.org/10.1038/s41422-021-00490-0.

1007 Zhang, L., Narayanan, K.K., Cooper, L., Chan, K.K., Devlin, C.A., Aguhob, A., Shirley, K., Rong,

1008 L., Rehman, J., Malik, A.B., et al. (2022). An engineered ACE2 decoy receptor can be

1009 administered by inhalation and potently targets the BA.1 and BA.2 omicron variants of SARS-

1010 CoV-2. BioRxiv https://doi.org/10.1101/2022.03.28.486075.

1011 Zheng, S.Q., Palovcak, E., Armache, J.-P., Verba, K.A., Cheng, Y., and Agard, D.A. (2017).

1012 MotionCor2: anisotropic correction of beam-induced motion for improved cryo-electron

1013 microscopy. Nat. Methods *14*, 331–332. https://doi.org/10.1038/nmeth.4193.

1014 Zhou, T., Tsybovsky, Y., Gorman, J., Rapp, M., Cerutti, G., Chuang, G.-Y., Katsamba, P.S.,

1015 Sampson, J.M., Schön, A., Bimela, J., et al. (2020a). Cryo-EM Structures of SARS-CoV-2 Spike

1016 without and with ACE2 Reveal a pH-Dependent Switch to Mediate Endosomal Positioning of

1017 Receptor-Binding Domains. Cell Host Microbe *28*, 867-879.e5.

1018 https://doi.org/10.1016/j.chom.2020.11.004.

1019 Zhou, X.X., Bracken, C.J., Zhang, K., Zhou, J., Mou, Y., Wang, L., Cheng, Y., Leung, K.K., and

1020 Wells, J.A. (2020b). Targeting Phosphotyrosine in Native Proteins with Conditional, Bispecific

1021 Antibody Traps. J. Am. Chem. Soc. *142*, 17703–17713. https://doi.org/10.1021/jacs.0c08458.

1022 Zhu, X., Mannar, D., Srivastava, S.S., Berezuk, A.M., Demers, J.-P., Saville, J.W., Leopold, K.,

1023 Li, W., Dimitrov, D.S., Tuttle, K.S., et al. (2021). Cryo-electron microscopy structures of the

1024 N501Y SARS-CoV-2 spike protein in complex with ACE2 and 2 potent neutralizing antibodies.

1025 PLoS Biol. *19*, e3001237. https://doi.org/10.1371/journal.pbio.3001237.

1026 Zost, S.J., Gilchuk, P., Case, J.B., Binshtein, E., Chen, R.E., Nkolola, J.P., Schäfer, A., Reidy,

1027 J.X., Trivette, A., Nargi, R.S., et al. (2020). Potently neutralizing and protective human

1028 antibodies against SARS-CoV-2. Nature *584*, 443–449. https://doi.org/10.1038/s41586-020-

1029 2548-6.